JOURNAL OF GEOPHYSICAL RESEARCH, VOL. 113, D08104, doi:10.1029/2007JD009115, 2008

Tropospheric transport climate partitioned by surface origin and transit time

Mark Holzer[1,2,3,4] and Timothy M. Hall[5,6]

Received 1 July 2007; revised 24 August 2007; accepted 16 October 2007; published 17 April 2008.

[1] We perform the first analysis of tropospheric transport using the global boundary propagator Green function, $\mathcal{G}$, which partitions air at every point and time according to both the transit time since last surface contact and the location of that contact. We compute $\mathcal{G}$ for a 3-year period with the MATCH model driven by NCEP reanalyses. Last contact time is resolved in 3-d intervals, and last-contact location is resolved with a global tiling of 41 patches concentrated in the Northern Hemisphere. The transport climate is quantified for four midlatitude receptor regions in terms of the seasonal mean surface-origin and transit-time partitioning of the column burden, the surface flux of newly arriving air, and the distribution of air mass in transit from source to receptor surface. At long transit times a nearly receptor-independent pattern of last-contact location is governed by where air is injected into the upper troposphere by deep convection and the high terrain of Tibet. The receptor origin composition of the column burden changes only slowly after $\sim$40 d for winter and fall, while the composition of the flux onto the receptor continues to change at $\sim$60 d. European and SE Asian air contribute comparably to the flux onto eastern North America, in spite of SE Asian air having the dominant burden. The flux of European air onto SE Asia in winter and fall is larger than the flux of SE Asian air onto Europe. The surface-to-surface transport mass distribution, $\mathcal{R}$, is used to identify transit-time-dependent source-receptor teleconnections.

Citation: Holzer, M., and T. M. Hall (2008), Tropospheric transport climate partitioned by surface origin and transit time, *J. Geophys. Res.*, *113*, D08104, doi:10.1029/2007JD009115.

1. Introduction

[2] Long-range intercontinental transport of pollutants and particulates is an emerging and growing threat to global air quality. This has been highlighted by transpacific transport of Asian pollutants to North America [e.g., *Cooper et al.*, 2004; *Jaffe et al.*, 1999, 2003; *Berntsen et al.*, 1999], which is anticipated to become increasingly important for North American air quality as east Asia continues rapid industrialization [*Jacob et al.*, 1999]. Likewise, North American pollutants have the potential to impact Europe [e.g., *Stohl and Trickl*, 1999; *Huntrieser et al.*, 2005], and European pollutants have the potential to add to an already poor situation in Asia [e.g., *Newell and Evans*, 2000; *Stohl et al.*, 2002; *Jaeglé et al.*, 2003]. The intercontinental transport of mineral dust across the Pacific and Atlantic oceans is also well documented [e.g., *Husar et al.*, 2001; *Prospero et al.*, 1981; *Prospero*, 1999], as are episodes of long-range pollutant transport in the Southern Hemisphere [e.g., *Wenig et al.*, 2002].

[3] Because of the episodic nature of long-range transport [e.g., *Yienger et al.*, 2000], most of the studies cited have focused on analyzing particular transport events or on transport during particular field campaigns (for an overview, see *Jacob et al.* [2003] and *Parrish et al.* [2004]). The statistical properties of the year-round intercontinental transport, which comprise the transport climate, have received comparatively less attention. Model-based studies of the climatological properties of intercontinental transport have focused primarily on transpacific transport [e.g., *Liu et al.*, 2005; *Liang et al.*, 2004, 2005; *Holzer et al.*, 2003, 2005; *Holzer and Hall*, 2007], with only the study by *Stohl et al.* [2002] taking a global perspective. The study by *Stohl et al.* [2002] analyzes ideal Lagrangian tracers that are tagged according to six broad continental regions of origin and that have the source structure of industrial carbon monoxide (CO) emissions. By contrast, the global distribution of various chemicals is now routinely computed with near-real-time simulations using the GEOS-CHEM model [*Bey et al.*, 2001; also http://www-as.harvard.edu/chemistry/trop/geos/], but the role of transport in these models is typically analyzed using only simple back trajectories for particular events [e.g., *Heald et al.*, 2003].

[1]Department of Applied Physics and Applied Mathematics, Columbia University, New York, New York, USA.
[2]Also at Atmospheric Science Program, Department of Earth and Ocean Sciences, University of British Columbia, Vancouver, British Columbia, Canada.
[3]Also at Physics Department, Langara College, Vancouver, British Columbia, Canada.
[4]Also at NASA Goddard Institute for Space Studies, New York, New York, USA.
[5]NASA Goddard Institute for Space Studies, New York, New York, USA.
[6]Also at Department of Applied Physics and Applied Mathematics, Columbia University, New York, New York, USA.

0148-0227/08/2007JD009115$09.00

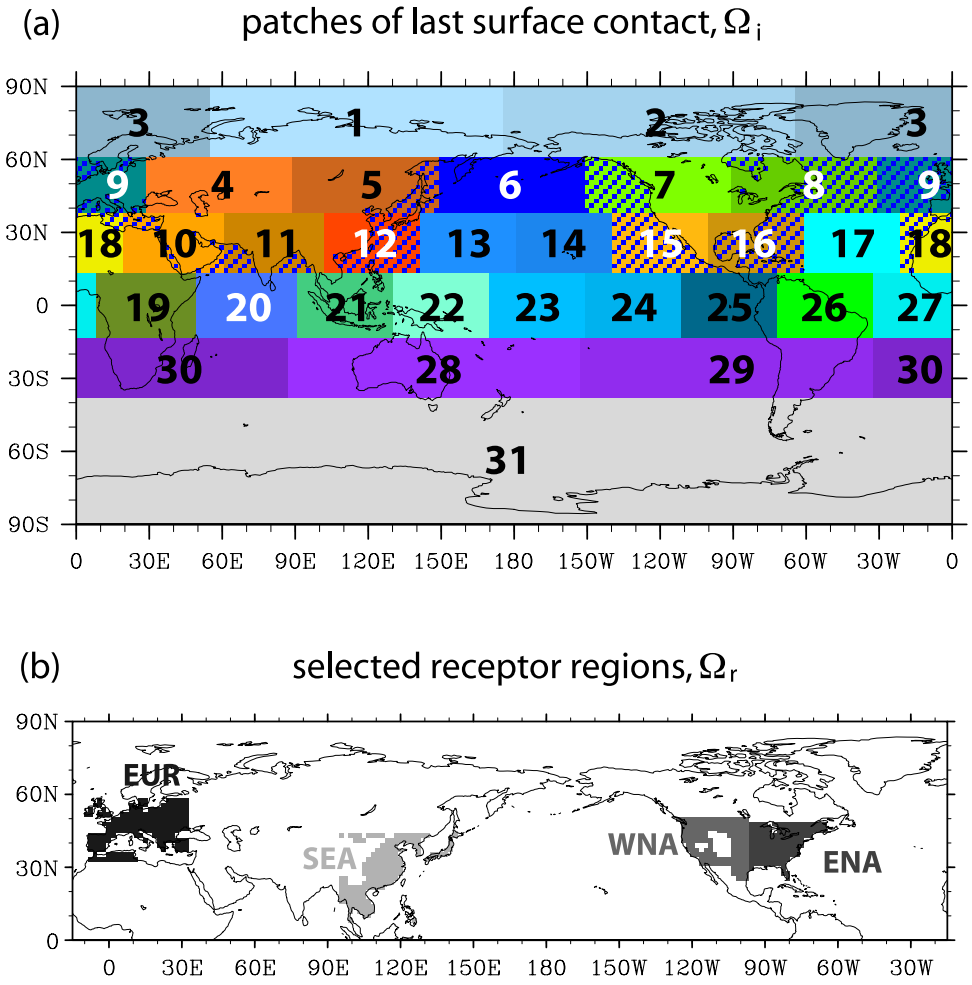

Figure 1. (a) The last-contact patches Ω_i used. In units of 10^7 km^2, the area A_i of patch Ω_i is $A_1 \ldots A_3 = 1.069$, $A_4 \ldots A_9 = 1.093$, $A_{10} \ldots A_{11} = 1.129$, $A_{12} \ldots A_{17} = 1.078$, $A_{18} = 1.129$, $A_{19} \ldots A_{20} = 1.348$, $A_{21} \ldots A_{26} = 1.287$, $A_{27} = 1.348$, $A_{28} \ldots A_{30} = 3.285$, and $A_{31} = 9.768$. The ten midlatitude patches Ω_5, Ω_7–Ω_{12}, Ω_{15}, Ω_{16}, and Ω_{18} have been partitioned into separate land and ocean patches, as indicated by the blue hatching. The percentages of the land area, L_i, of these patches are $L_5 = 80$, $L_7 = 61$, $L_8 = 38$, $L_9 = 39$, $L_{10} = 79$, $L_{11} = 77$, $L_{12} = 36$, $L_{15} = 25$, $L_{16} = 28$, and $L_{18} = 72\%$. (b) The receptor regions, Ω_r, considered for this study: Europe (EUR), Southeast and east Asia (SEA), midlatitude western North America (WNA), and midlatitude eastern North America (ENA). In units of 10^7 km^2, the receptor regions have areas $A_{\mathrm{EUR}} = 0.5508$, $A_{\mathrm{SEA}} = 0.5880$, $A_{\mathrm{WNA}} = 0.4640$ (0.5530 if terrain above 1800 m elevation is not excluded), and $A_{\mathrm{ENA}} = 0.4363$.

[4] In this paper, we take an entirely tracer-independent approach to diagnosing global tropospheric transport. Our goal is to isolate the role of transport from all the other factors influencing the concentration of particular trace species, such as chemistry, deposition, and the temporal and spatial variability of sources. (Deposition could be considered to be part of the transport in our diagnostic framework, but we will not do so here.) We quantify transport by calculating at every point $\mathbf{r}$ in the atmosphere the mass fraction $\mathcal{G}(\mathbf{r}, t|\Omega_i, t')dt'$ of air at time t that had last contact during time interval $(t', t' + dt')$ with surface patch Ω_i, for a global tiling of such patches (Figure 1a). Air is thus partitioned according to both when and where it had last surface contact. This represents a natural extension of the transit-time distribution [e.g., *Holzer et al.*, 2003] to the joint distribution $\mathcal{G}(\mathbf{r}, t|\Omega_i, t')$ of times t' and places Ω_i since last surface contact. The distribution $\mathcal{G}$ is also the boundary propagator (a type of Green function) for spatially varying surface mixing ratio [*Holzer and Hall*, 2000], and hence constitutes a complete description of transport from the Earth's surface. Such boundary propagators have recently been used to quantify oceanic transport [e.g., *Haine and Hall*, 2002; *Primeau*, 2005; *Peacock and Maltrud*, 2006], where the assumption of steady flow greatly reduced the complexity of the problem. Our study here represents the first calculation of the global boundary propagator $\mathcal{G}$ for the highly variable and turbulent flow of the troposphere. By precisely labeling air according to when and where it last had surface contact, $\mathcal{G}$ provides a rigorous definition of air mass, a concept typically used only qualitatively in mete-

orology because of the constant presence of mixing. Because $\mathcal{G}$ naturally incorporates the integrated effect of mixing, a surface-origin labeled air mass is always unambiguously defined.

[5] Green functions exploit the linearity of passive tracers to reduce the determination of their mixing ratios to a simple linear superposition of precomputable functions. For tracers of surface origin, one can either use a flux Green function [e.g., *Holzer*, 1999; *Stohl et al.*, 2002] or, as we do here, a mixing ratio Green function ("boundary propagator"). (The work of *Stohl et al.* [2002] does not explicitly use Green functions, but their method is essentially equivalent.) The flux Green function is the response to pulses of surface emission fluxes that are followed by a zero-flux boundary condition, while the boundary propagator is the response to pulses in surface mixing ratio followed by a zero-mixing-ratio boundary condition. Tracer mixing ratios can be synthesized using flux Green functions from a knowledge of the surface emissions, or using boundary propagators from a knowledge of the surface mixing ratio. The relationships between the two types of Green function, and their physical interpretation as distributions was explored by *Holzer and Hall* [2000].

[6] Mixing ratio and flux Green functions capture different aspects of transport that complement each other. The flux Green function captures all possible paths from the injection site, including paths along the surface, and allows surface mixing ratio to be attributed to particular emissions. The global boundary propagator tracks air since last surface contact by resetting labels of surface origin with every surface contact, and allows mixing ratio in the interior of the atmosphere to be attributed to where the air last made surface contact and the surface mixing ratio there. The flux Green function is physically a puff of passive tracer that has infinite lifetime after injection, so that a tracer-specific chemical decay time or other removal/cutoff process must be invoked to obtain normalized distributions of time since injection. Here we focus on the global boundary propagator because it has the compelling interpretation as a naturally tracer-independent normalized joint distribution of times and places since last surface contact. The global boundary propagator also provides a new transport diagnostic, namely the flux with which air from polluted remote boundary layers first arrives on a given receptor surface. Because the boundary propagator is the Green function for surface mixing ratio and not for emission sources, and because surface mixing ratio will be smoother than the sources, we do not make any assumptions about the source structure and tile the Earth's surface with a set of last-contact patches that is nearly uniform in the Northern Hemisphere, except for additional land-ocean partitioning.

[7] We emphasize that our goal is to diagnose, in a tracer-independent manner, the atmosphere's transport from and to the surface, and not to simulate any particular chemical species. We calculate $\mathcal{G}$ for 3 years (September 1998 to August 2001) using a global atmospheric transport model driven by NCEP reanalysis data. The resulting partitioning of air parcels into time and place of last surface contact is available at every point in the atmosphere and analyzed in terms of the seasonal mean climatology. For definiteness we illustrate our results for four specific receptor regions (Figure 1b). We establish the transport climate as quantified in terms of the transit-time and surface-origin partitioning of the column burden above the receptor regions, the flux of newly arriving air onto the receptor surfaces, and the mass fraction of the atmosphere in transit from source to receptor.

[8] In the interpretation of passive tracers, and in particular of boundary propagators whose evolution is sensitive to mixing to the surface, it is helpful to describe the position of tracer plumes relative to isentropes, surfaces of constant potential temperature. This will be done throughout because many atmospheric mixing processes, such as Rossby wave breaking and the flow associated with frontal systems, tend to be nearly adiabatic so that much atmospheric transport is organized along isentropes [e.g., *Plumb and Mahlman*, 1987]. In the terminology of *Hoskins* [1991], the evolution of the boundary propagator therefore depends strongly on whether or not air finds itself in the Underworld, the part of the atmosphere whose isentropes intersect the Earth's surface. (*Hoskins* [1991] further classifies the part of the atmosphere whose isentropes cross the tropopause as the Middleworld, above which lies the Overworld.)

2. Boundary Propagator $\mathcal{G}$

2.1. Defining Properties

[9] Given a tiling of the Earth's surface with patches Ω_i, the mass fraction of air at point $\mathbf{r}$ and time t that had last contact with Ω_i during time interval $(t', t' + dt')$ is given by $\mathcal{G}(\mathbf{r}, t|\Omega_i, t')dt'$, where $\mathcal{G}$ satisfies the source-free passive-tracer equation

$$\frac{\partial}{\partial t}(\rho\mathcal{G}(\mathbf{r}, t|\Omega_i, t')) + \nabla \cdot \mathbf{J}(\mathbf{r}, t|\Omega_i, t') = 0, \tag{1}$$

subject to the boundary conditions

$$\mathcal{G}(\mathbf{r}, t|\Omega_i, t') = \begin{cases} \delta(t - t') & \text{if } \mathbf{r} \in \Omega_i, \\ 0 & \text{otherwise.} \end{cases} \tag{2}$$

In (1) the flux $\mathbf{J}(\mathbf{r}, t|\Omega_i, t') \equiv \rho\mathbf{u}\mathcal{G}(\mathbf{r}, t|\Omega_i, t') + \mathbf{J}_{sg}(\mathbf{r}, t|\Omega_i, t')$ is the sum of the advective flux $\rho\mathbf{u}\mathcal{G}$ and the flux $\mathbf{J}_{sg}$ due to subgrid parameterizations such as convection and turbulent diffusion.

[10] The mass fraction $\mathcal{G}dt'$ is also a boundary propagator, that is, a Green function for surface mixing ratio, χ_s, so that

$$\chi(\mathbf{r}, t) = \sum_i \int_{-\infty}^{t} dt'\, e^{-(t-t')/\tau_c}\mathcal{G}(\mathbf{r}, t|\Omega_i, t')\chi_s(\Omega_i, t'), \tag{3}$$

where we have inserted the term $\exp[-(t - t')/\tau_c]$ to account for a decaying species with a fixed lifetime τ_c. While we will not use (3) to synthesize mixing ratios at interior points from surface mixing ratios, χ_s, in this paper, the chemical lifetime τ_c sets the timescale for the transit times $t - t'$ over which $\mathcal{G}$ must be known to construct such a synthesis. In (3) it is assumed that the surface mixing ratio on the Ω_i patch, $\chi_s(\Omega_i, t')$, does not vary spatially over Ω_i. This assumption is not a fundamental limitation, because the patches Ω_i can be shrunk to infinitesimal size [*Holzer and Hall*, 2000]. In practice, however, finite computational resources necessitate a modest number (41 in this study) of

surface patches. The boundary propagator is normalized so that

$$\sum_i \int_{-\infty}^{t} dt' \, \mathcal{G}(\mathbf{r}, t|\Omega_i, t') = 1, \tag{4}$$

which is the physical statement that if we go back far enough in "source time" t', air at ($\mathbf{r}$, t) must have had contact somewhere with the surface. Equation (4) underlines that $\mathcal{G}$ has the probabilistic interpretation of being the joint distribution of place Ω_i and transit time $\tau = t - t'$ since last surface contact. Specifically, $\mathcal{G}(\mathbf{r}, t|\Omega_i, t')dt'$ is the probability that a fluid element at ($\mathbf{r}$, t) had last surface contact during (t', $t' + dt'$) at Ω_i. For convenience we will also refer to $\mathcal{G}(\mathbf{r}, t|\Omega_i, t')dt'$ as "Ω_i air" or, more completely as "(Ω_i, t') air," at ($\mathbf{r}$, t) of "age" or transit time $\tau = t - t'$. For clarity it is also useful to refer to t as "field time" and to t' as "source time."

2.2. Transport Mass Distribution $\mathcal{R}$

[11] The surface fluxes of the boundary propagator allow us to calculate the mass fraction, $\mathcal{R}d\tau$, of the atmosphere that is in transit from Ω_i to first subsequent contact on Ω_r, partitioned according to the Ω_i-to-Ω_r transit time, τ. The patch-to-patch transit time, τ, is also the residence time in the atmosphere between successive surface contacts. Physically, $\mathcal{R}(\tau, \Omega_i, \Omega_r; t)d\tau$ is the mass fraction of the atmosphere in transit at time t whose residence time will lie in the interval $\tau \in (\tau, \tau + d\tau)$, and we refer to $\mathcal{R}$ as the transport mass distribution [see also *Primeau and Holzer*, 2006; *Holzer and Primeau*, 2006]. The distribution $\mathcal{R}$ is of interest as a fundamental transport diagnostic, and also because it places an upper limit on the time for which the transport mass fraction will be subject to chemical transformations before making surface contact.

[12] The mass fraction $\mathcal{R}(\tau, \Omega_i, \Omega_r; t)d\tau$ can be calculated [*Primeau and Holzer*, 2006] as the flux of Ω_i air that will be flushed onto the Ω_r receptor surface in time τ, that is,

$$\mathcal{R}(\tau, \Omega_i, \Omega_r; t) = \frac{1}{M} \int_{t-\tau}^{t} dt' \int_{\Omega_r} d\mathbf{a} \cdot \mathbf{J}(\mathbf{r}_s, t' + \tau|\Omega_i, t'), \tag{5}$$

where M is the total (dry) mass of the atmosphere and $d\mathbf{a}$ is the area element oriented into the ground at surface location $\mathbf{r}_s$ on Ω_r. We may consider $\phi \equiv \frac{1}{\tau}\int_{t-\tau}^{t} dt' \int_{\Omega_r} d\mathbf{a} \cdot \mathbf{J}$ to be the ($t - \tau$)-to-t averaged, receptor-integrated flux (per unit residence time) of air that had last contact with Ω_i and that will make its first subsequent surface contact with Ω_r after residing in the atmosphere for $\tau \in (\tau, \tau + d\tau)$. Equation (5) then states that $\phi = M\mathcal{R}/\tau$, which is the residence-time partitioned analogue of the familiar statement that the flux through a fluid domain equals the resident mass divided by the residence time.

[13] The transport mass distribution has the normalization

$$\sum_r \sum_i \int_0^{\infty} d\tau \mathcal{R}(\tau, \Omega_i, \Omega_r; t) = 1, \tag{6}$$

where it is assumed that we have a complete tiling (with nonoverlapping patches) of the globe with both last-contact patches Ω_i and with first-contact receptor patches Ω_r. If the entire Earth's surface is denoted by Ω, the normalization (6) can alternatively be expressed as $\int_0^{\infty} d\tau \, \mathcal{R}(\tau, \Omega, \Omega; t) = 1$.

2.3. Model and Diagnostic Design

[14] To compute $\mathcal{G}$, we use MATCH (Model of Atmospheric Transport and Chemistry), a three-dimensional global model of the atmosphere developed by *Rasch et al.* [1997] that uses the mass-conserving SPITFIRE (Split Implementation of Transport using Flux Integral Representation) flux algorithm [*Rasch and Lawrence*, 1998]. We drive MATCH with T62 NCEP reanalysis data [*Kalnay et al.*, 1996; *Kistler et al.*, 2001] on a Gaussian grid of 94 latitudes and 192 longitudes ($\sim 1.9^\circ \times 1.9^\circ$), with 28 hybrid levels up to $\sim$3 mbar. While the NCEP data provides strong observational constraints, it must be kept in mind that convection and boundary layer mixing are parameterized so that there is still potential for model biases. A nonlocal scheme is used to compute the boundary layer height below which a profile of vertical diffusion coefficients is prescribed [*Rasch et al.*, 1997], and convection is parameterized by combining a local diffusive scheme [*Hack*, 1994] with a nonlocal penetrative scheme [*Zhang and McFarlane*, 1995].

[15] The distribution $\mathcal{G}(\mathbf{r}, t|\Omega_i, t')$ is calculated with the delta function of (2) replaced by a 3-d-long square pulse on Ω_i of amplitude $1/\Delta t'$, with $\Delta t' = 3$ d, which is equivalent to computing a 3-d average of the δ function response over t'. On the surface other than Ω_i (and on Ω_i after the mixing ratio pulse ceases) zero mixing ratio is enforced. Physically, the pulse imparts an (Ω_i, t') label to air in contact with Ω_i during (t', $t' + \Delta t'$), and the zero-mixing-ratio boundary conditions ensure that this label is removed upon repeat surface contact. This removal of the (Ω_i, t') label is crucial because we wish to bin fluid elements according to when and where they had last surface contact regardless of where they were prior to that last contact. The boundary conditions are implemented by specifying the mixing ratio for the lowest model level.

[16] The contact patches Ω_i used for this study are shown in Figure 1a. The patches essentially constitute a coarse-resolution grid covering the Northern Hemisphere. The 27 latitude-longitude bounded patches north of $\sim$13°S have roughly equal area of $\sim 10^7$ km^2. The ten midlatitude patches, Ω_5, Ω_7–Ω_{12}, Ω_{15}, Ω_{16}, and Ω_{18}, which contain both significant land and ocean areas, are further subdivided into separate land and ocean patches, so that transport from the very different terrestrial and oceanic boundary layers can be distinguished. The land and ocean portions of Ω_i will be denoted Ω_i^L and Ω_i^O. Except for the land-ocean partitioning, no particular source structure has been built into the tiling, so that the composition of air in terms of last surface contact is not specific to any particular chemical species.

[17] We archive 3-d averages of $\mathcal{G}(\mathbf{r}, t|\Omega_i, t')$ and daily averages of the corresponding meteorological fields for t from 1 September 1998 to 31 August 2001 and transit times, or ages, $\tau = t - t'$ up to 60 d. With $\tau \leq 60$ d our propagators are relevant to the intercontinental transport of species with chemical lifetimes less than $\sim$2 months (e.g., ozone, light nonmethane hydrocarbons, CO), but slower pathways involving interhemispheric exchange or transport through the stratosphere, which are relevant for long-lived species such as CFCs and methane, are not captured.

[18] The resulting data set is very rich and high-dimensional, consisting of ~15,000 three-dimensional tracers, each of which evolves over 60 d of transit time (twenty 3-d averages). In addition to "field point and time," $(\mathbf{r}, t)$, we have the transit-time variable $\tau = t - t'$ and the 41 discrete spatial variables Ω_i (31 latitude-longitude bounded patches, 10 of which are subdivided into land and ocean components) identifying the patch of last surface contact.

[19] The high-dimensional character of the data set places limitations on what aspects of the general character of the boundary propagator can reasonably be presented in a single paper. Although $\mathcal{G}$ is available at every point in the atmosphere, and we can therefore analyze any receptor region, we focus for economy of presentation and definiteness on the receptor regions shown in Figure 1b. These regions were chosen to be over land and to roughly coincide with the high population densities of the midlatitudes. Mountainous terrain above 1800 m elevation has been excluded for the WNA patch when computing fluxes into the surface to eliminate the contribution from the free troposphere. To further streamline our analysis we focus primarily on the composition of the seasonally averaged column burden over each receptor and on the seasonally averaged flux of newly arriving air onto the surface. The standard deviation of the interannual variability of the seasonal mean receptor averaged burdens and fluxes is roughly 5–10%. Here we focus on the climatological seasonal means, that is, on the seasonal means averaged over the three available years. An analysis of variability on 3-d to monthly timescales is deferred to a future study.

3. Seasonal Mean Column Burden and Surface Flux Composition

[20] We adopt the conventional 3-months definitions for the seasons: DJF, MAM, JJA, and SON. The mass fraction in a 3-d transit-time interval is given by $\Delta t'\,\mathcal{G}$, where $\Delta t' = 3$ d (this follows from our broadened 3-d pulsed boundary condition). Mass fractions over larger transit-time bands are calculated by summing over 3-d intervals. Seasonal climatological averages, denoted by brackets $\langle \ldots \rangle$, are determined for each transit time $t - t'$ by averaging $\mathcal{G}(\mathbf{r}, t|\Omega_i, t')$ over the field times t within the seasons of all 3 years at fixed $t - t'$.

3.1. Column Burden

[21] The column burden per unit area, B, of Ω_i air in a 3-d transit-time interval is calculated as $B(\mathbf{r}_s,\ t|\Omega_i,\ t') \equiv \Delta t' \int_0^{p_s(\mathbf{r}_s,t)} \mathcal{G}(\mathbf{r}, t|\Omega_i, t')dp/g$, where p_s is surface pressure, $g = 9.81$ m s^{-2}, and $\mathbf{r}_s$ is the surface location of the column. The total column burden in a 3-d transit-time interval, regardless of where last surface contact occurred, is given by $\sum_i B(\mathbf{r}_s,\ t|\Omega_i,\ t')$. The fractional contribution to the total climatological, receptor-area averaged burden from air that had last contact with patch Ω_j during $(t',\ t' + \Delta t')$ is given by $\left\langle \overline{B(\mathbf{r}_s, t|\Omega_j, t')} \right\rangle / \sum_i \left\langle \overline{B(\mathbf{r}_s, t|\Omega_i, t')} \right\rangle$, where the overbar denotes the area average over the receptor region.

[22] Figure 2 shows maps of the percentage contribution from each contact patch of Figure 1a to the WNA-averaged climatological burden as it evolves with increasing transit time. To visually compensate for the differing areas of the land and ocean components of land-ocean partitioned patches, Ω_i, their land (ocean) percentage has been multiplied for plotting purposes by $A(\Omega_i)/A(\Omega_i^L)$ (by $A(\Omega_i)/A(\Omega_i^O)$), where $A(\Omega)$ is the area of Ω. (An area-weighted average of the land and ocean percentages scaled in this manner gives the percentage of the total patch.) At early transit times the WNA-averaged burden is dominated by contact patches that overlap with the WNA region. This is expected physically because air that had recent surface contact must come from nearby. With increasing transit time one sees pronounced seasonal differences in how the contact patches with the largest contributions move upwind. During DJF and MAM, vigorous mixing along sloping isentropes keeps the midlatitude troposphere well in contact with the surface. Consequently, for DJF, MAM, and SON the dominant contact patches are seen to move westward from WNA across the Pacific surface as transit time increases from 4 to 12 d. By contrast, during JJA the Pacific troposphere is very stable [e.g., *Holzer and Hall*, 2007] and relatively little air over WNA had last contact with the Pacific surface. The dominant JJA contact patches therefore tend to jump from North America to the east Asian surface. This is consistent with the fact that summertime transpacific transport occurs primarily aloft and is fed by convective injection over the Asian land mass [e.g., *Stohl et al.*, 2002; *Holzer et al.*, 2005].

[23] With increasing transit time there is no zonal homogenization of the contact regions, with localized clusters of patches being the main contributors to the burden for transit times up to the 60 d studied. While a plume of tracer-labeled air will be zonally homogenized in the free troposphere, the contributions from each surface patch Ω_i are determined by (1) how effective the Ω_i air is in escaping the boundary layer during the mixing ratio pulse before zero-mixing-ratio boundary conditions are enforced, and by (2) the efficiency of vertical mixing in bringing Ω_i air in contact with the surface while in transit to the receptor. Because boundary layer mixing is highly inhomogeneous, with strong land-sea contrast, a zonal strip of patch distribution cannot develop for any transit time.

[24] At the longest transit times available of $\tau \sim 2$ months, just a few tropical (DJF and MAM) or subtropical (JJA and SON) contact patches dominate (Figure 3a). For a given season, the long-τ patterns of the surface origin are nearly identical for the four midlatitude receptors. We can understand the emergence of these nearly receptor-independent patterns as follows: After contact with the high-latitude Ω_i patches, most fluid elements can isentropically be mixed back to the surface, so that only a small fraction of the high-latitude Ω_i air remains in the atmosphere for longer than 48 d without surface contact. What we see at long transit times is, by construction, air that has remained in the atmosphere for a long time without surface contact. Thus, the dominant contribution to the burdens at long transit times comes from air that has been injected deep into the tropical troposphere. This is consistent with the fact that the patterns of Figure 3a match patterns of the model's deep convection shown in Figure 3b. For JJA and SON, surface air also appears to be injected into the upper troposphere from the high terrain of the Tibetan plateau. (The model's coarse-grained surface pressure there falls below 500 mbar.)

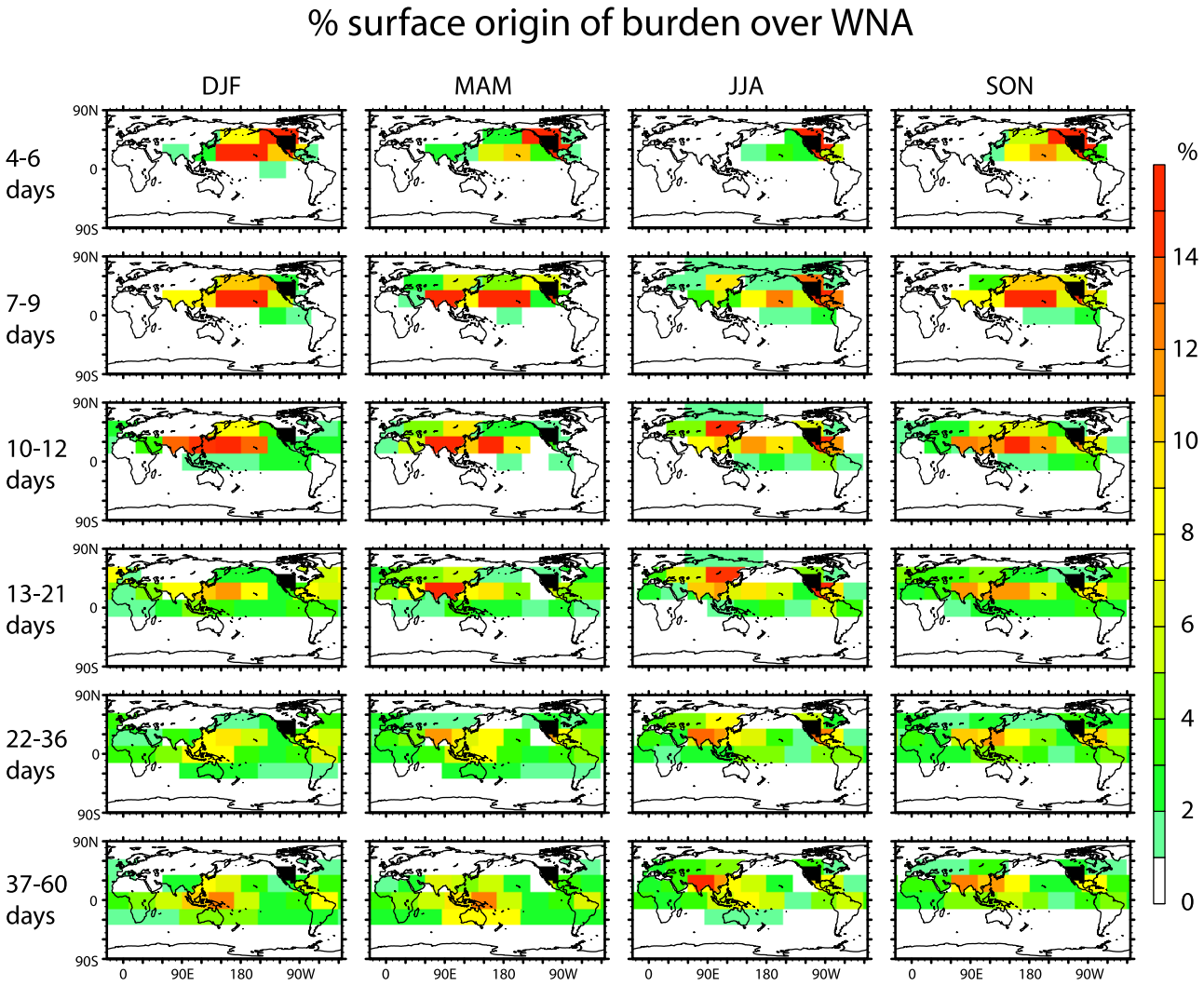

Figure 2. Evolution with transit time since last surface contact of the percentage contribution from each contact patch Ω_i to the seasonal mean, WNA-averaged column burden. For the patches partitioned into land and ocean parts, the percentage is multiplied by the area of the patch divided by the area of the land or ocean part, respectively, so that an area-weighted average of the land and ocean parts gives the combined land-ocean total for the patch. The contribution has been integrated over the transit-time intervals indicated to the left. The WNA receptor region is indicated in black.

[25] While the plots of Figures 2 and 3a directly show the geographical origin of the air for a given receptor and transit-time band, these kind of plots are inefficient in showing the detailed evolution of the composition of the burden with transit time. We therefore take advantage of the relatively small number of contact patches and show in Figure 4a the evolution with transit time of the percentage contribution from each contact patch to the seasonal mean, receptor-averaged column burden for each receptor and season. The corresponding evolution with transit time of the total column burden regardless of surface origin, $\sum_i \left\langle \overline{B(\mathbf{r}_s, t|\Omega_i, t')} \right\rangle$, is qualitatively similar for all receptors and hence shown in Figure 4b only for the WNA receptor. The large total burdens at early times are dominated by air that had last surface contact with patches overlapping the receptor. Seasonal differences can be seen at early times, with the burden highest in JJA when air can most efficiently escape the surface. However, during JJA thick continental boundary layers over the receptors also cause air to be efficiently mixed down to the surface, so that the burden decays rapidly with increasing transit time. For all seasons the burden decays more gradually after ~10 d, as air from all source patches begins to contribute to the burden. Ultimately all air from all contact patches will have made surface contact, ensuring that the column burden eventually decays to zero.

[26] Figure 4a shows that for all seasons the dominance of the contributions from the several contact patches that overlap with the receptor is broken after approximately 9 d (given our 3-d time resolution), long enough for the local air to be either swept out of the receptor column, or to make surface contact. During DJF and MAM, substantial (10–20% by τ = 60 d) contributions from the Southern Hemisphere (SH) subtropical patches are visible. During JJA and SON, SH contributions are negligible. The combined contributions from the SH and equatorial patches correspond in

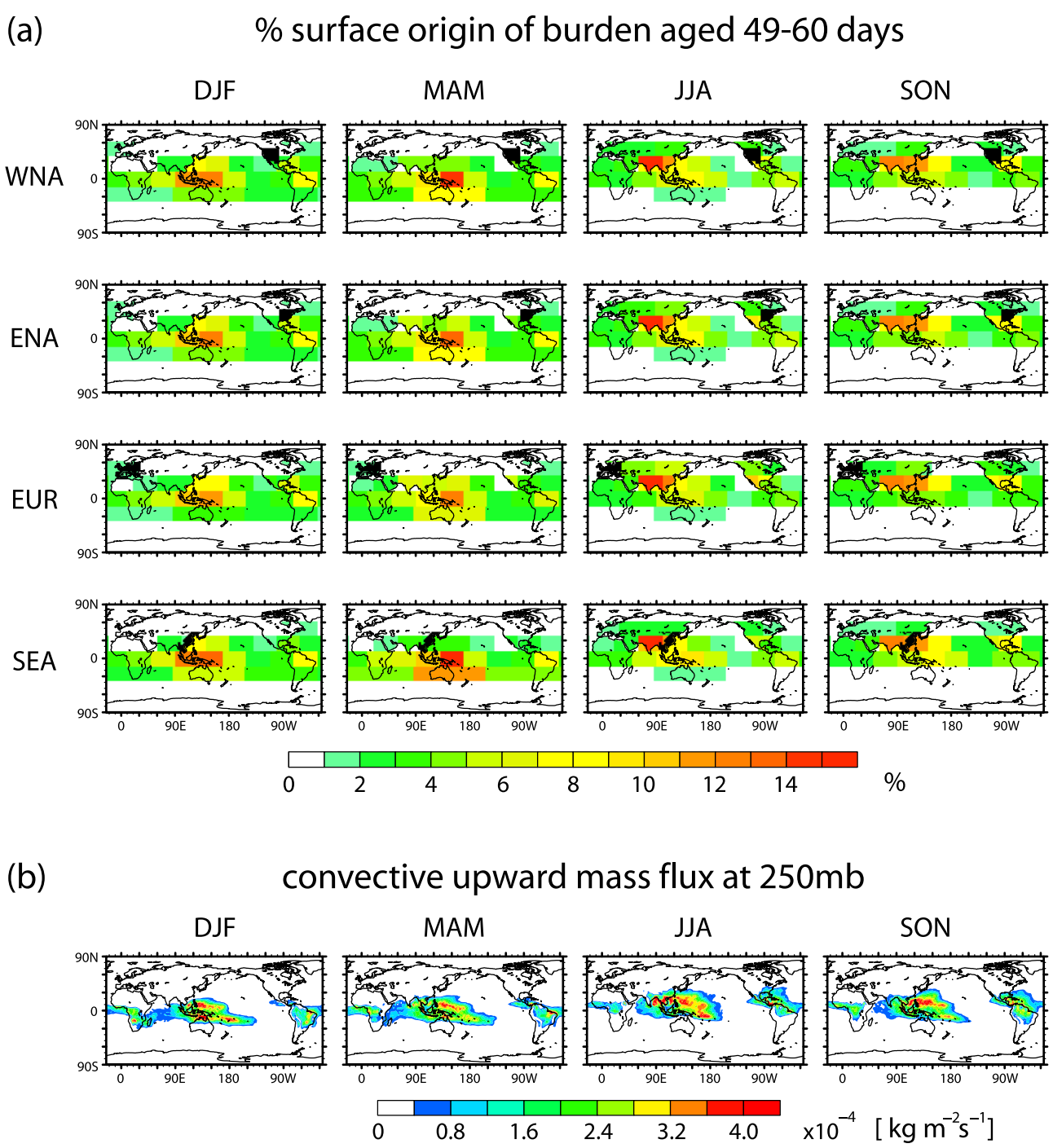

Figure 3. (a) The long-time (integrated over the 49–60 d transit-time interval) seasonal mean percentage contribution from each contact patch Ω_i to the receptor-averaged column burden, plotted as for Figure 2. Note that for a given season, the pattern is only weakly dependent on receptor. The receptor regions are indicated in black. (b) The seasonal mean convective upward mass flux at 250 mbar as calculated using the MATCH implementation of the parameterization by *Zhang and McFarlane* [1995].

Figure 4a to the width of the region between the yellow "Saharan" Ω_{18} band and the 100% line (top of the plots). By τ = 60 d, these patches contribute approximately 60–70% for DJF, 70–80% for MAM, 40–50% for JJA, and 30–40% for SON, for all receptors with the largest contributions for SEA, the most southern of our receptors. Contributions to the burden from Arctic Ω_1, Ω_2, and Ω_3 air are small for all seasons and receptors, but visible for EUR and ENA at ~5% and $\tau \sim 9$–21 d for JJA, and at earlier transit times for the other seasons.

[27] The dashed lines on Figure 4a partition the air from the Northern Hemisphere midlatitude patches into the fractions that had last contact with either land (band positioned below the dashed line) or ocean (band positioned

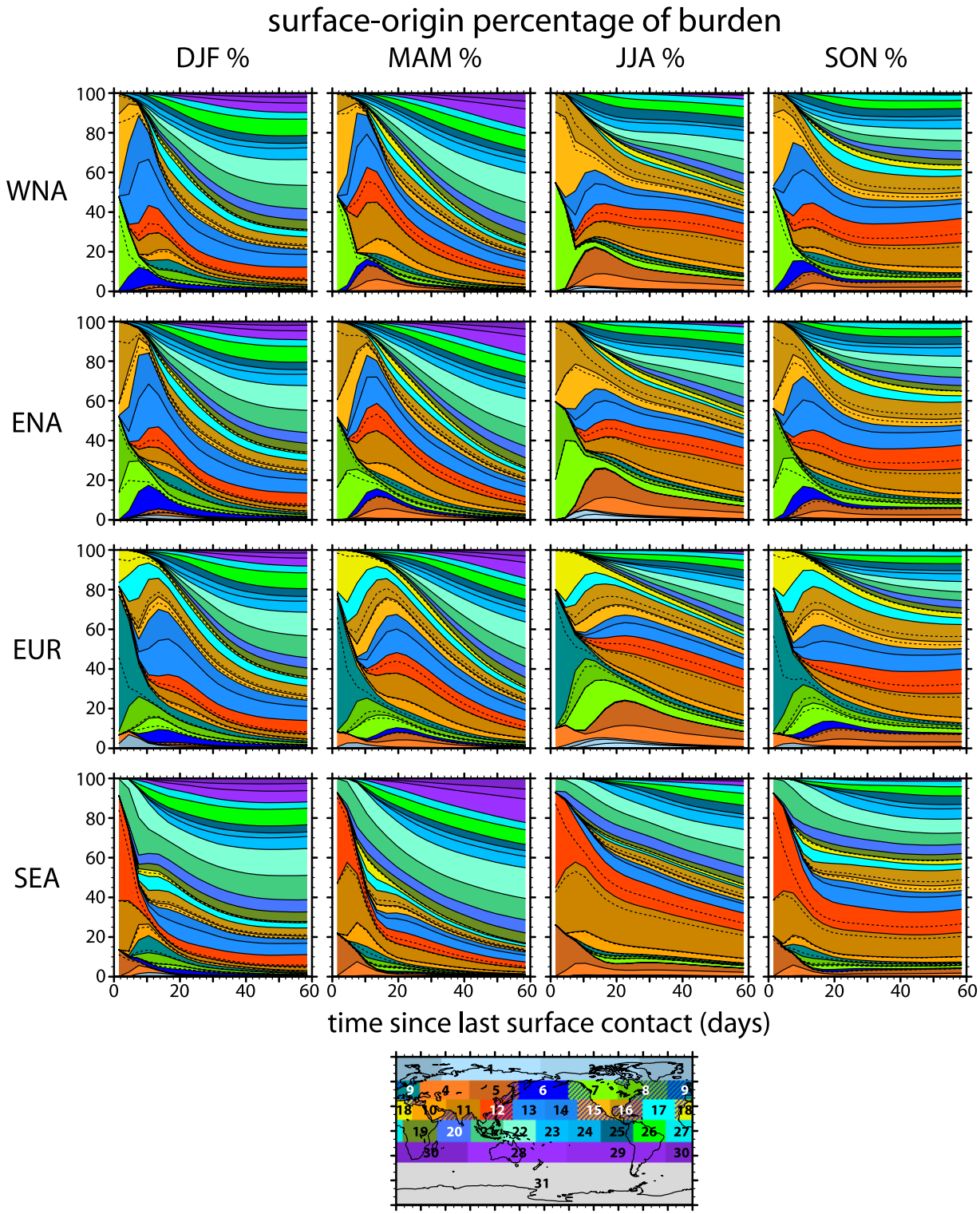

Figure 4a. Seasonal mean surface-origin partitioning of the receptor-averaged column burden as a function of time since last surface contact. The vertical width of each colored band gives the percentage contribution from the corresponding surface patch, as indicated by the color mapping. The percentages are stacked sequentially from the Ω_1 to Ω_{31} contribution. The dashed lines subdivide bands into contributions that had last surface contact with the land (below the dashed line) and ocean (above the dashed line) parts of the surface patch.

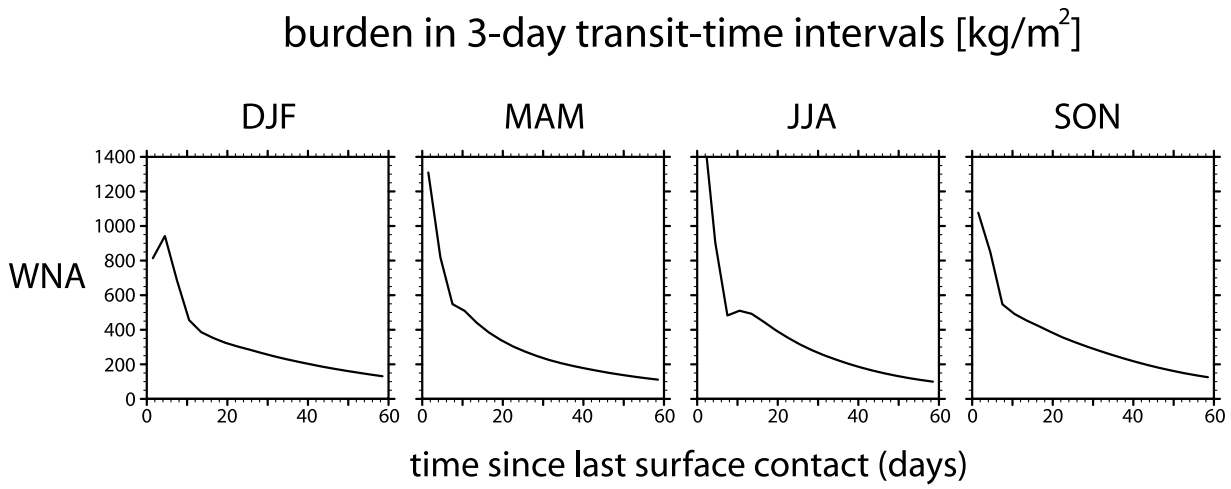

Figure 4b. Total WNA-averaged, seasonal mean column burden in each 3-d transit-time interval as a function of transit time since last surface contact for the seasons indicated.

above the dashed line). For the northern continental patches Ω_5 (Siberia), Ω_7 and Ω_8 (North America), and Ω_9 (Europe), the land component dominates in summer, while the ocean component dominates in winter, as expected from the seasonal land-sea contrast of the boundary layer. Shallow wintertime boundary layers, virtually no convection, and regional subsidence (e.g., Siberia) over land inhibit surface air entering the free troposphere. The burdens of SE Asian Ω_{12} air are divided about equally between land and ocean contributions in summer, consistent with convection taking place over both the land and ocean parts of Ω_{12}. In winter convection over Indochina does not completely shut down, and the wintertime last-ocean contact fraction of Ω_{12} air is only about twice as large as the land fraction. Air that had last surface contact on the Ω_{16} patch (SE North American and Caribbean) is nearly equally divided into land and ocean contributions in summer, while the ocean contributions dominate in winter. Over the oceanic parts of Ω_{12} and Ω_{16} frontal lifting onto warm conveyor belts occurs during all seasons [*Stohl*, 2001], consistent with the substantial ocean component of air from these patches over remote receptors for all seasons. For the SW North American Ω_{15} patch and the western Saharan Ω_{18} patch, the land portion dominates in summer, while land and ocean contributions are nearly equal in winter. This is consistent with the fact that the oceanic parts of these patches include the subtropical highs of the North Pacific and North Atlantic, which are regions of subsidence. For the Middle Eastern and south Asian patches, Ω_{10} and Ω_{11}, the land component dominates during all seasons.

[28] For DJF and SON the composition of the burden changes only slowly after ~40 d (although the total burden continues to decay with transit time), while for MAM and JJA the composition still changes at $\tau = 60$ d because of the growing contribution of the tropical and SH air, with the greatest changes of ~0.5%/d for the EUR receptor. Because SH and tropical air must be transported aloft to the middle and high latitudes (that is, to the Underworld) before having isentropic access to the surface, this air contributes at longer transit times. During DJF and SON isentropes intersecting the Northern Hemisphere surface have their greatest southward extent, consistent with the more rapid equilibration of the tropical and SH air mass fraction in those seasons.

[29] In Figure 5 we show the receptor-averaged column burdens, $\left\langle \overline{B(\mathbf{r}_s, t|\Omega_i^L, t')} \right\rangle$, of air that had last surface contact with the land surface, Ω_i^L, of selected contact patches as a function of transit time, $t - t'$. We focus on the "industrial patches," covering Europe (Ω_9^L), SE Asia (Ω_{12}^L), and midlatitude North America (Ω_7^L and Ω_8^L), that are likely to be in contact with polluted boundary layer air. For clarity we do not show the contribution from the industrial patches that overlap with the receptor, the emphasis being on long-range transport from remote source regions. While the combination of Figures 4a and 4b contains the information of Figure 5, the transit-time dependence of the burden can be seen directly in Figure 5 and shows the following features:

[30] For the North American receptors WNA and ENA, the dominant remote "industrial" air is Ω_{12}^L air from SE Asia, with the largest contributions in spring at a transit time of ~9–12 d, consistent with previous studies of transpacific transport [e.g., *Jaffe et al.*, 1999; *Holzer et al.*, 2003; *Heald et al.*, 2006]. The smaller contribution of European Ω_9^L air is similar for the WNA and ENA receptors, with a mode at ~18 d by which time the Ω_9^L air has experienced a significant degree of zonal homogenization so that WNA and ENA see approximately equal burdens. Eastern North American Ω_8^L air and European Ω_9^L air make comparable contributions to the WNA column in JJA, but for the other seasons the European contribution is significantly larger at its mode. This is consistent with the fact that the Ω_8^L air traverses the storm track regions of both the Atlantic and the Pacific on its circumglobal journey to WNA, while the Ω_9^L air traverses only the Pacific. At the entrance to the storm tracks, there tends to be vigorous vertical mixing with relatively thick wintertime boundary layers where air makes surface contact with the ocean and hence looses its identity as air that had last surface contact over land. We also note that the WNA burden of eastern North American Ω_8^L air has a bimodal transit-time distribution. The fast mode corresponds to the climatological Ω_8^L air mass spreading out and

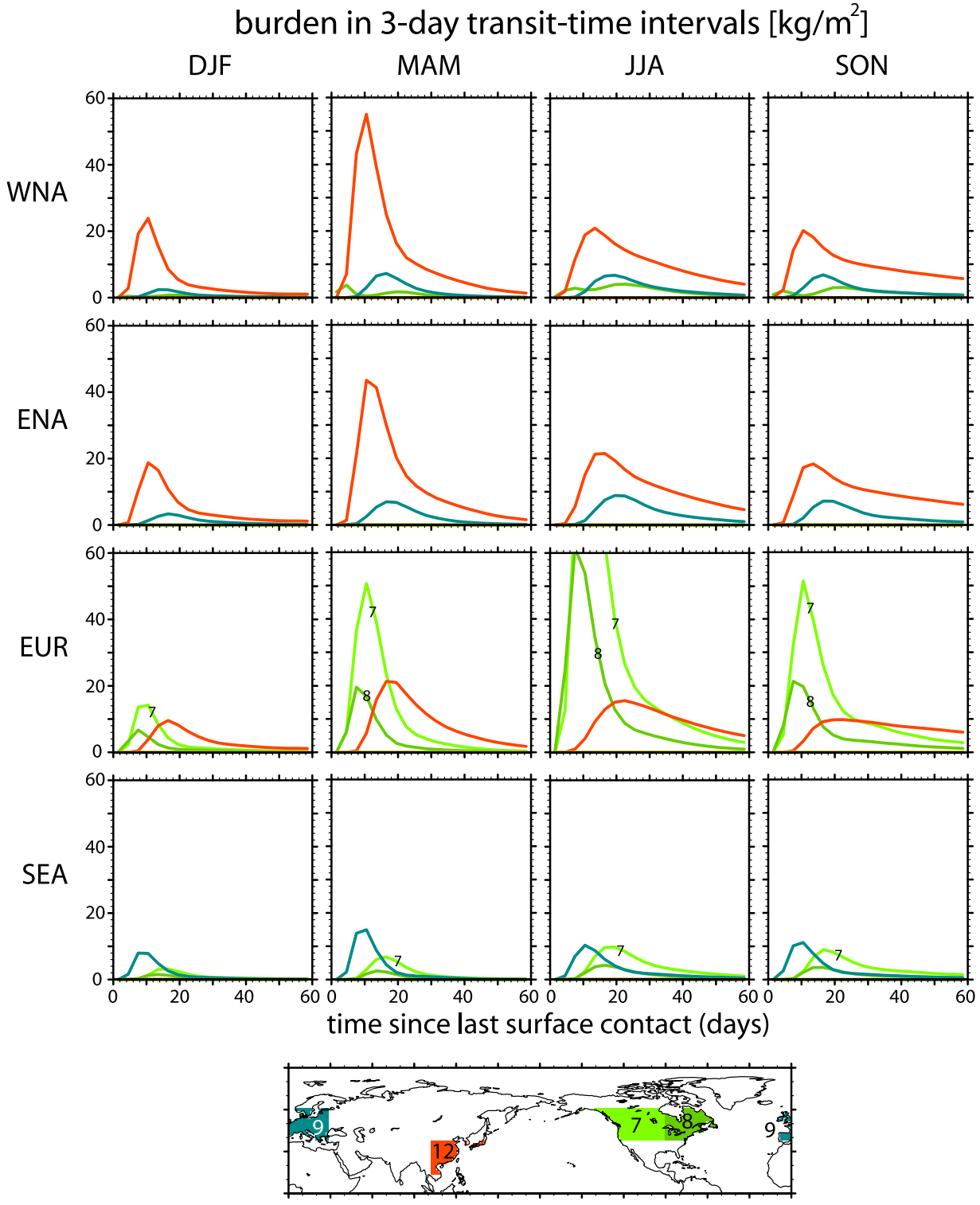

Figure 5. Transit-time partitioned, receptor-averaged column burden in each 3-d transit-time interval of air that had last contact with the four color-coded "industrial" contact patches, for the seasons and receptors indicated. These industrial patches are the land surface of patches Ω_7, Ω_8, Ω_9, and Ω_{12}. Contributions from contact patches overlapping or abutting the receptor region have been excluded for clarity.

quickly entering the nearby WNA receptor to the west. The westward part of this spreading is the mixing signature of weather systems with easterly flow, such as subpolar highs. The slow mode corresponds to westerly transport around the globe, followed by subsequent mixing from the Arctic southward along sloping isentropes.

[31] In the EUR column, east Asian Ω_{12}^L air has its mode at $\tau \sim 18-21$ d (fastest in DJF and MAM), and is thus $\sim$9 d older than in the WNA and ENA columns. Compared to WNA and ENA, the Ω_{12}^L air signal in the EUR column is least attenuated in JJA and SON, consistent with most of the Ω_{12}^L air being injected into the upper Middleworld during JJA and SON, so that it tends to stay in the upper troposphere. The greatest attenuation is seen in DJF when much of the Ω_{12}^L air travels in the Underworld, where isentropic mixing to the surface continually removes the Ω_{12}^L label. The evolution of Ω_{12}^L air in MAM is intermediate between that of DJF and JJA. The dominant industrial contributions to the EUR burden during all seasons, except DJF, come from American Ω_7^L and Ω_8^L air, at a mode of $\tau \sim 6-12$ d, fastest for the closer Ω_8^L. This is expected since in this case the receptor is immediately downwind of the American source patches. Transport of North American air to EUR is weakest in winter because a lack of convection over the source patches causes much less air to escape the surface to attain long transit times, and the air that does escape finds itself entering the Atlantic storm tracks, where relatively efficient mixing to the surface continues to remove the Ω_7^L and Ω_8^L labels.

[32] The SEA receptor column sees comparable contributions from European Ω_9^L and American Ω_7^L and Ω_8^L air for JJA and SON, while European air is the dominant industrial contributor in DJF and MAM. European air at a mode of $\sim$10 d is transported about a week faster than North American air, which has to traverse the Atlantic en route to SEA. Much American air is advected toward the pole giving much lower burdens over SEA than over EUR. For DJF and MAM, the mode of both the European and American air comes from a plume that traverses Asia to the northern edge of SEA. The younger plume of European air is more coherent and has greater amplitude than the American air, which experiences more dispersion and vertical mixing to the surface as it crosses the Atlantic. Consequently, European air dominates American air in the burden over SEA for DJF and MAM.

[33] The SEA burdens of European Ω_9^L air show modest seasonality, with the burden at the mode of its distribution being largest in MAM. This contrasts with the strong seasonality seen by *Newell and Evans* [2000] in the percentage of 5-d back trajectories from 100°E and 20–60°N that pass through the European boundary layer, with the winter percentage being an order of magnitude larger than the summer percentage. This apparent discrepancy is reconciled by the fact that the global boundary propagator and simple back trajectories are very different diagnostics. The back trajectories of *Newell and Evans* [2000] were not subjected to subgrid vertical mixing, trajectories that made contact with the boundary layer en route across Asia were not excluded from being of European origin, and 5 d is too short to sample the transit-time distribution of European air over SEA. By contrast, the boundary propagator integrates both advection and parameterized subgrid diffusion and convection, removes the Ω_9^L label from European air when it makes subsequent surface contact, and partitions air according to time since last surface contact. The SEA burdens of air that had last surface contact with Europe, rigorously computed from the global boundary propagator, have weaker and differently phased seasonality than suggested by the statistics of simple 5-d back trajectories.

[34] Before leaving this section on receptor burdens, we comment briefly on the evolution of the $\mathcal{G}$ plumes with transit time. Qualitatively, the climatological evolution of Ω_i^L air from the industrial patches is similar to the evolution of the CO-like tracer described by *Stohl et al.* [2002], and the evolution of Ω_{12}^L air is similar to the evolution of east Asian air studied by *Holzer et al.* [2003, 2005] for different boundary conditions. However, the quantitative transit-time dependence of the global boundary propagator depends critically on the interaction of the surface-origin labeled air with mixing processes that can bring it into surface contact. This essential physical difference between the global boundary propagator and other transport diagnostics satisfying different boundary conditions precludes meaningful quantitative comparison. The global boundary propagator and other diagnostics provide complementary transport information and do not represent different ways of diagnosing the same information.

3.2. Surface Flux of Newly Arriving Air

[35] We have examined the column burden of air above the receptor regions. Much of the remote air contributing to this burden passes overhead without affecting the surface. The boundary propagator can also diagnose the transport to the Earth's surface, where the impact of air from remote sources on air quality is of greatest concern. However, $\mathcal{G}$ itself is not useful for this purpose, but rather the flux of $\mathcal{G}$ onto the surface. At the surface, $\mathcal{G}(\mathbf{r_s}, t|\Omega_i, t')$ itself is uninteresting because, by definition, air at the surface has had its last contact with the local surface during the current contact pulse of duration $\Delta t'$, and $\mathcal{G}$ reduces to simple pulses in time for each Ω_i as expressed by the boundary conditions (2). Therefore, local surface air has no contribution from remote contact patches or even from local air aged beyond $\Delta t'$. However, the continuous resetting of the (Ω_i, t') label at the surface by the boundary conditions implies a flux onto the surface of newly arriving Ω_i air, that is, Ω_i air that makes surface contact for the first time since last surface contact with Ω_i. The flux of newly arriving air has both local and remote contributions and is a natural diagnostic of long-range transport to the surface. While the primary quantity of interest for air quality is the surface mixing ratio, the flux of air newly arriving from polluted remote boundary layers also has clear implications for air quality. There are also transport problems for which the flux of constituents into the surface is of primary interest. An example is the determination of the flux of bioavailable iron from the atmosphere into the ocean [e.g., *Luo et al.*, 2005].

[36] We note in passing that the boundary propagators studied by *Holzer et al.* [2003, 2005] and *Holzer and Hall* [2007] quantified transport from a single source region, Ω, and satisfied boundary conditions different from those considered here, namely mixing ratio pluses on Ω, but zero flux outside of Ω. Such hybrid boundary conditions allow Ω air on the surface outside of Ω, so that air can be partitioned

nontrivially even at the surface according to its time since last Ω contact. However, such single-Ω boundary propagators cannot be used to partition air according to both time and place since last surface contact because the hybrid boundary conditions do not permit the superposition (3) over different Ω_i.

[37] The flux of Ω_i air in a 3-d transit-time interval newly arriving at surface point $\mathbf{r}_s$ is given by $F(\mathbf{r}_s, t|\Omega_i, t') \equiv \Delta t' \, \mathbf{n} \cdot \mathbf{J}(\mathbf{r}_s, t|\Omega_i, t')$, where $\mathbf{n}$ is the surface normal oriented into the ground. In practice the flux of $\mathcal{G}$ onto the surface, $\mathbf{n} \cdot \mathbf{J}$, is computed as the mass of (Ω_i, t') air that is removed per model time step, per unit area, when enforcing zero surface mixing ratio. We will now examine the flux of newly arriving air paralleling our discussion for the burden.

[38] Figure 6a shows the surface-to-surface transit-time dependence of the fractional contribution of Ω_i air to the total climatological, receptor-area averaged mass flux of air onto the surface. The fractional contribution to the flux is calculated as $\left\langle \overline{F(\mathbf{r}_s, t|\Omega_i, t')} \right\rangle / \sum_j \left\langle \overline{F(\mathbf{r}_s, t|\Omega_j, t')} \right\rangle$. The transit-time dependence of the total flux, $\sum_j \left\langle \overline{F(\mathbf{r}_s, t|\Omega_j, t')} \right\rangle$, is qualitatively similar for all receptors, and we therefore show it only for WNA in Figure 6b. At the shortest residence time, the flux onto the receptor patch Ω_r is completely dominated by air that had its last contact with overlapping patches. One can show that in the continuum limit, $\mathbf{n} \cdot \mathbf{J}(\mathbf{r}_s, t|\Omega_i, t')$ has a physical singularity at $t = t'$ at surface receptor points $\mathbf{r}_s$ on Ω_i [*Holzer and Hall*, 2000; *Hall and Holzer*, 2003; *Primeau and Holzer*, 2006]. The physical cause of the singularity is (eddy) diffusion. On the small scales the diffusion imparts a jittery back-and-forth component to the motion of fluid elements, which may be regarded as undergoing a random walk. Thus, as the continuum limit of ever smaller "steps" is approached at constant diffusivity, fluid elements make an ever-increasing number of contacts with the surface during any finite time interval [*Hall and Holzer*, 2003]. Because of this singularity, we plotted the total flux of Figure 6b on a log scale.

[39] The total flux is largest in summer and spring (particularly for WNA and EUR (not shown)). This reflects the fact that during JJA and MAM deep daytime boundary layers form over these receptors, which provide conduits for efficiently mixing air from aloft to the surface. In fact, we find that maps (not shown) of the total flux onto the surface correlate strongly with maps of MATCH's seasonal mean prognostic boundary layer height, $\langle h_{\mathrm{pbl}} \rangle$, for all seasons and transit times studied. The squared spatial correlation coefficient ranges from $r^2 \sim 0.25$ to $r^2 \sim 0.82$, depending on season and transit-time interval. The receptors with the largest $\langle h_{\mathrm{pbl}} \rangle$ are EUR (from Spain and Greece) and WNA (from the southwestern USA). While $\langle h_{\mathrm{pbl}} \rangle$ is a predictor for the total flux, its surface-origin partitioning depends on the integrated effect of transport from the Ω_i patches and cannot be deduced solely from $\langle h_{\mathrm{pbl}} \rangle$.

[40] The land-ocean partitioning of the flux (indicated by the dashed line) is broadly similar to that of the burden. While there are quantitative differences, generally where the land portion dominates the burden it also dominates the flux, suggesting that the vertical profiles of the land and ocean contributions are generally not drastically different over remote receptors at the modes of the distributions.

[41] A comparison of Figures 4a and 6a for short transit times shows that the several source patches that overlap the receptor patch make nearly the same percentage contributions to the flux as they do to the column burden. This is expected from the fact that for infinitesimally short mixing ratio pulses, the partitioning of burden and flux must be identical in the limit of zero transit time. For very short transit time, Ω_i air is just above the surface and on the surface itself the mixing ratio is set to zero. Therefore, the diffusive flux onto the surface (proportional to the vertical gradient) is proportional to the mixing ratio just above the surface, and the surface-origin partitioning must be the same for both burden and flux in the limit of zero time since last surface contact.

[42] Transport to the receptor surface is slower than transport to the free troposphere above the receptor. Therefore, in contrast to the surface-origin partitioning of the burden, the partitioning of the flux is still rapidly changing at $\tau = 60$ d for all receptors and seasons. Unlike for the burden, Arctic air makes a significant contribution to the surface flux for ENA and EUR, and visible contributions for the other receptors. This reflects the fact that the midlatitude surface is well connected to the northern latitudes through the sloping isentropes of the Underworld. While the mass of air that arrives from the Arctic is a small contributor to the burden, this mass arrives near the surface resulting in substantial contributions to the flux of newly arriving air. Similarly, air from patches Ω_4 (central Asia) and Ω_9 (Europe) makes a larger fractional contribution to the surface flux than it does to the burden. Conversely, air from patches like Ω_{12} (SE Asia) that is injected convectively into the Middleworld during summer and fall, and hence isentropically isolated from the surface, makes smaller fractional contributions to the surface flux than it does to the burden.

[43] The contrast between burden and surface flux is particularly clear in the transit-time partitioned flux from individual contact patches. In Figure 7 we show the receptor-patch averaged flux, $\langle \overline{F} \rangle$, of newly arriving air from the same industrial patches (the land-only patches Ω_7^L, Ω_8^L, Ω_9^L, and Ω_{12}^L) for which we plotted the individual burdens. Overall Figure 7 shows a similar pattern for the fluxes as Figure 5 does for the burdens. This is in accord with the expectation that the flux onto the surface is proportional to the total amount present, to the degree to which the air masses from the different patches have similar vertical profiles. However, Figure 7 also shows important differences, and they are consistent with differences in the air masses' vertical distribution.

[44] Although SE Asian Ω_{12}^L air dominates the burden for WNA and ENA for all seasons, it only dominates the flux onto the surface for WNA during DJF, MAM, and JJA. For ENA during all seasons, and for WNA during SON, the fluxes of SE Asian Ω_{12}^L and European Ω_9^L air are comparable in magnitude, although the mode of the Ω_{12}^L flux occurs several days before the mode of the Ω_9^L flux, because the SE Asian tracer does not need to traverse the Asian continent en route to North America. Where the ratio of the Ω_{12}^L to Ω_9^L fluxes is similar to the ratio of the Ω_{12}^L to Ω_9^L burdens (WNA for DJF, MAM, and JJA), with Ω_{12}^L dominating Ω_9^L, the vertical profiles of the two air masses are similar. Where the Ω_{12}^L flux is comparable to, or less than, the Ω_9^L flux (ENA all

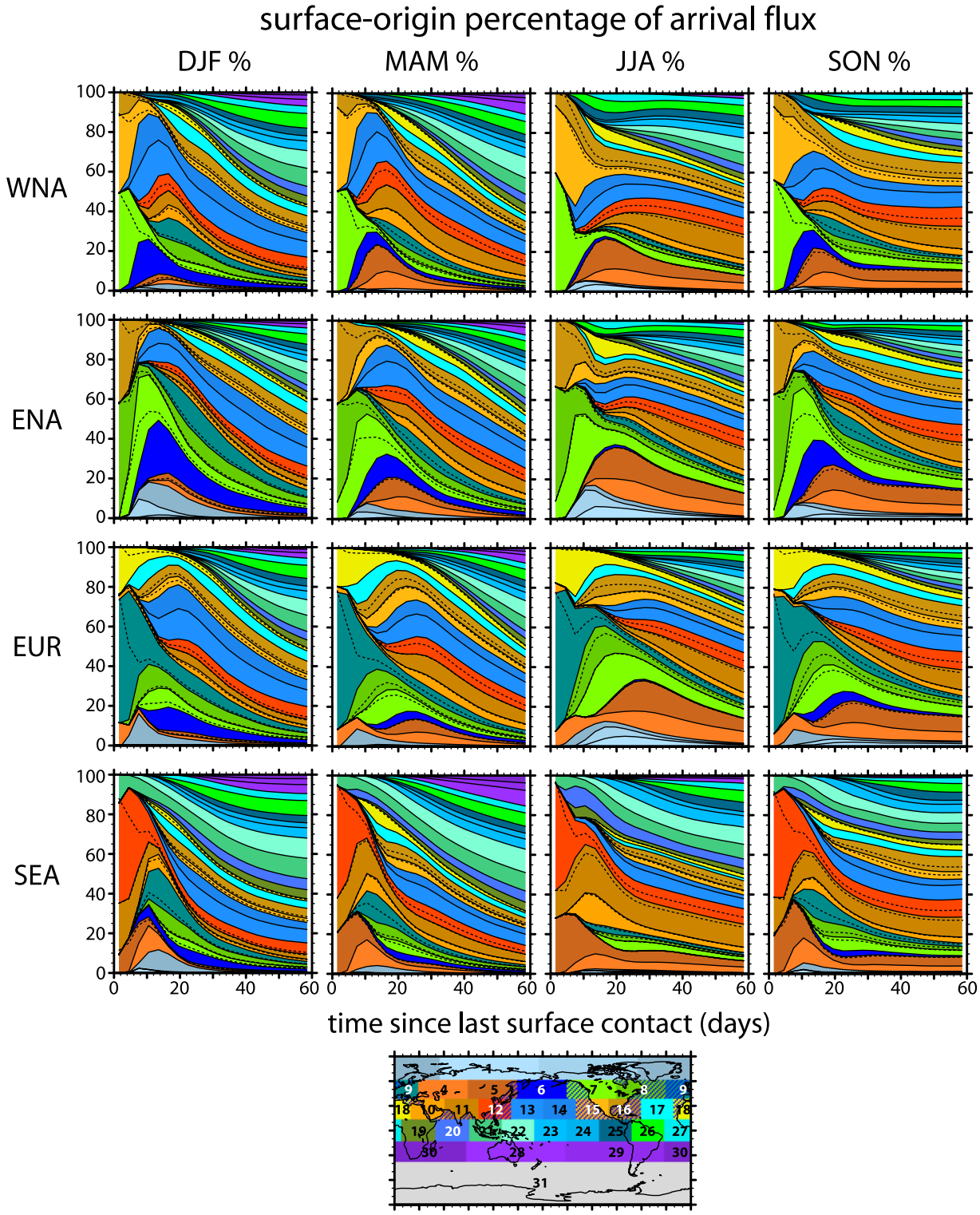

Figure 6a. Seasonal mean surface-origin partitioning of the flux of newly arriving air onto the receptor region indicated as a function of time since last surface contact. The vertical width of each colored band gives the percentage contribution from the corresponding surface patch, as indicated by the color mapping. The percentages are stacked sequentially from the Ω_1 to Ω_{31} contribution. The dashed lines subdivide bands into contributions that had last surface contact with the land (below the dashed line) and ocean (above the dashed line) parts of the surface patch.

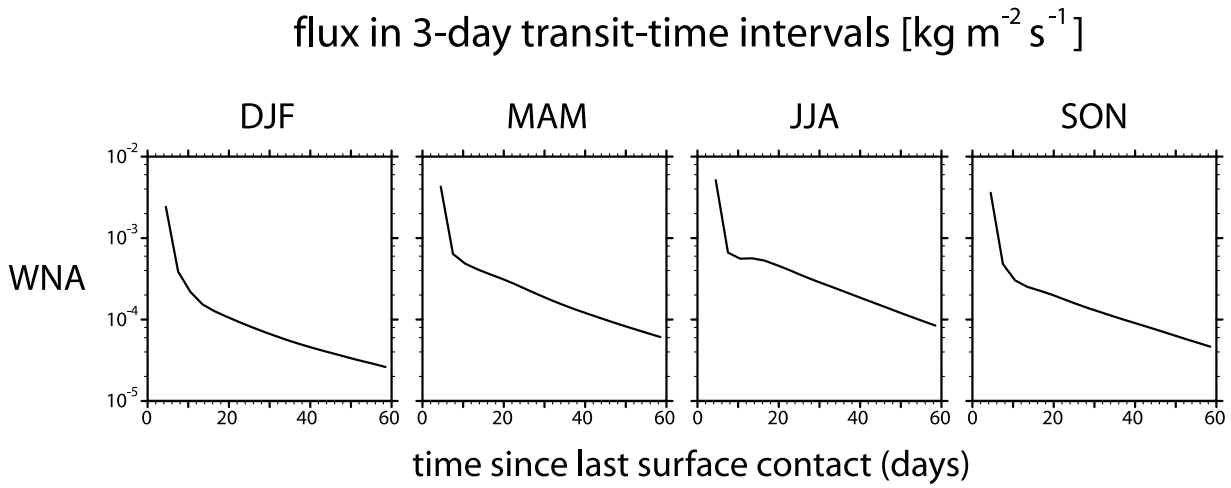

Figure 6b. Total WNA-averaged, seasonal mean flux of newly arriving air onto the WNA receptor surface in each 3-d transit-time interval for the seasons indicated.

seasons, WNA for SON), the Ω_{12}^L profile has most of its weight in the middle to upper troposphere, while the Ω_9^L air is located in the middle to lower troposphere, so that the Ω_9^L air has larger near-surface gradients in spite of having a smaller column burden. The implication is that European pollutants of a lifetime of ~20 d or longer can potentially arrive at the same rate on the ENA surface as SE Asian pollutants, given equal mixing ratios over the source patches.

[45] The flux of European Ω_9^L air onto SEA is nearly as large as the flux of SE Asian Ω_{12}^L air onto WNA and ENA, and at its mode for DJF and MAM significantly larger than the flux of Ω_{12}^L air onto EUR. For MAM, the Ω_9^L air arrives over SEA in the lower troposphere, so that the ratio of European to North American fluxes onto SEA is much larger that the corresponding ratio of the burdens. The mode of the Ω_{12}^L air flux onto EUR is at ~30 d, while the mode of the Ω_9^L air flux onto SEA occurs at ~10–15 d, reflecting the differing distances traveled via westerly flow.

[46] Finally we note that some of the flux curves display bimodality pointing to distinct transport mechanisms. The bimodality of the flux of Ω_8^L air into WNA is consistent with the bimodality of the column burden of Ω_8^L air over WNA (see Figure 5), with the early mode being accentuated in the flux because the WNA Ω_8^L air's eastward spread occurs at low levels, while the circumglobally transported air arrives in the middle and upper troposphere. The flux of Ω_9^L air onto ENA for MAM has a shoulder at ~10 d, which is due to full-fledged bimodality for MAM 2001. The early mode of the MAM 2001 Ω_9^L flux is due to rapid eastward transport across the Atlantic just south of Iceland and Greenland along the northern branch of cyclonic circulations, while the main mode results from circumglobally transported air. These Atlantic north easterlies do not bring sufficient Ω_9^L air to ENA to impart a short-time mode to the MAM 2001 column burden.

4. Transport Mass Distribution

[47] The transport mass distribution, $\mathcal{R}(\tau, \Omega_i, \Omega_r; t)$, developed in section 2.2 quantifies the mass of air at time t in transit from source patch Ω_i to receptor patch Ω_r, whose surface-to-surface transit time τ will be found to lie in the interval $(\tau, \tau + d\tau)$. Figure 8 shows maps of the climatological seasonal mean $\langle\mathcal{R}\rangle$ integrated over the residence-time bands indicated, for the example of $\Omega_r = \Omega_{\mathrm{WNA}}$ (the absolute contributions are shown, without any area weighting for the land-ocean partitioned patches). Figure 8 demonstrates that $\mathcal{R}$ is very effective in identifying $\Omega_i \rightarrow \Omega_r$ surface-to-surface transport teleconnections. At small τ, the transport mass destined for first surface contact on WNA is dominated by patches overlapping the receptor region, while with increasing τ remote patches upwind from the receptor contribute. Intercontinental surface-to-surface transport to WNA is strongest for MAM and JJA, with DJF and SON being several times smaller, consistent with the flux distributions of Figure 7. Siberian Ω_5^L air is the dominant contributor to the transport mass fraction in JJA, for residence times between ~2 and 4 weeks. In MAM, Ω_5^L air and western Pacific Ω_{13} air are important for residence times between ~2 and 3 weeks. With increasing τ, the largest contributions for MAM and JJA come from high-terrain and convectively injected south Asian Ω_{11}^L air.

[48] To explore systematically the residence-time dependence of $\mathcal{R}$ and the surface-to-surface teleconnections (without intermediate surface contact) it reveals, we plot in Figure 9 the mass fraction of the atmosphere in each 3-d residence-time interval, $\sum_i \langle\mathcal{R}(\tau, \Omega_i, \Omega_r; t)\rangle\, \Delta t'$, that makes first contact with the receptor patch, Ω_r, partitioned into color-coded contributions, $\langle\mathcal{R}(\tau, \Omega_i, \Omega_r; t)\rangle\, \Delta t'$, from each source patch Ω_i. (Unlike for Figures 4a, 4b, 6a, and 6b we do not separately plot the percentage contributions and the total to avoid having to visually multiply those curves to get the absolute magnitude of $\mathcal{R}$.) The total transport mass fraction regardless of surface origin, destined for a given receptor, $\sum_i \langle\mathcal{R}\rangle\, \Delta t'$, is the outer envelope of the curves of Figure 9. Because $\mathcal{R}$ is simply the flux onto the receptor accumulated for time τ (see section 2.2), the total transport mass fraction, like the total flux, is largest in summer and spring particularly for WNA and EUR (for WNA, see also Figure 8). As is the case for the total flux, maps (not shown) of $\sum_i \langle\mathcal{R}(\tau, \Omega_i, \Omega_r; t)\rangle\, \Delta t'$, with one grid cell of the map

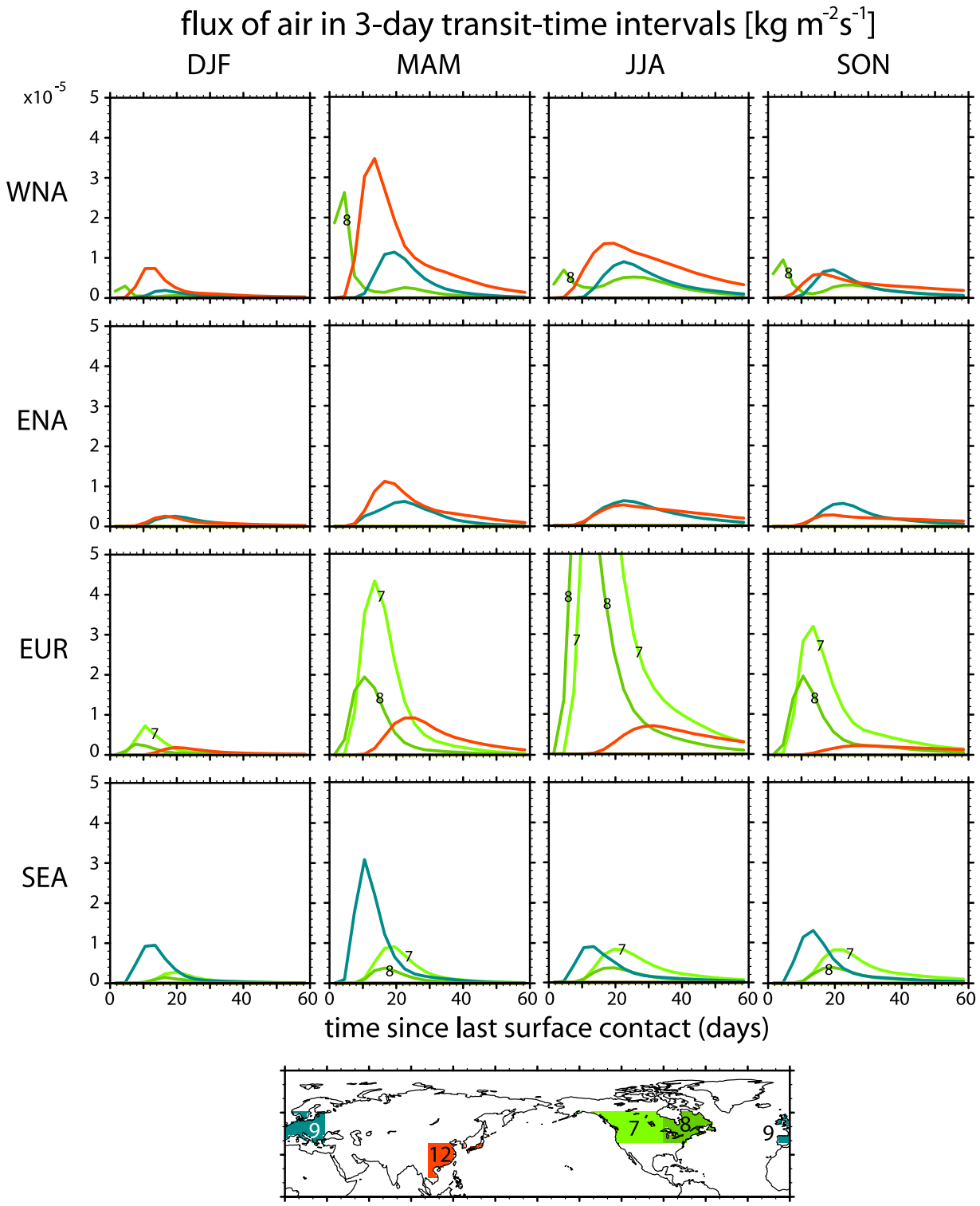

Figure 7. Transit-time partitioned, receptor-averaged flux of newly arriving air in each 3-d transit-time interval from the four color-coded "industrial" contact patches, for the seasons and receptors indicated. These industrial patches are the land surface of patches Ω_7, Ω_8, Ω_9, and Ω_{12}. Contributions from contact patches overlapping or abutting the receptor region have been excluded for clarity.

corresponding to Ω_r being a single grid cell of the model, correlate strongly ($r^2 \sim 0.25$ to $r^2 \sim 0.80$, depending on season and transit-time interval) with maps of MATCH's seasonal mean prognostic boundary layer height, $\langle h_{\mathrm{pbl}} \rangle$.

[49] The dominant teleconnections with the receptors can be identified in Figure 9 as the bands of $\langle \mathcal{R} \rangle \Delta t'$ with the largest vertical width. The largest mass fractions $\langle \mathcal{R} \rangle \Delta t'$ occur at short residence times for patches overlapping the

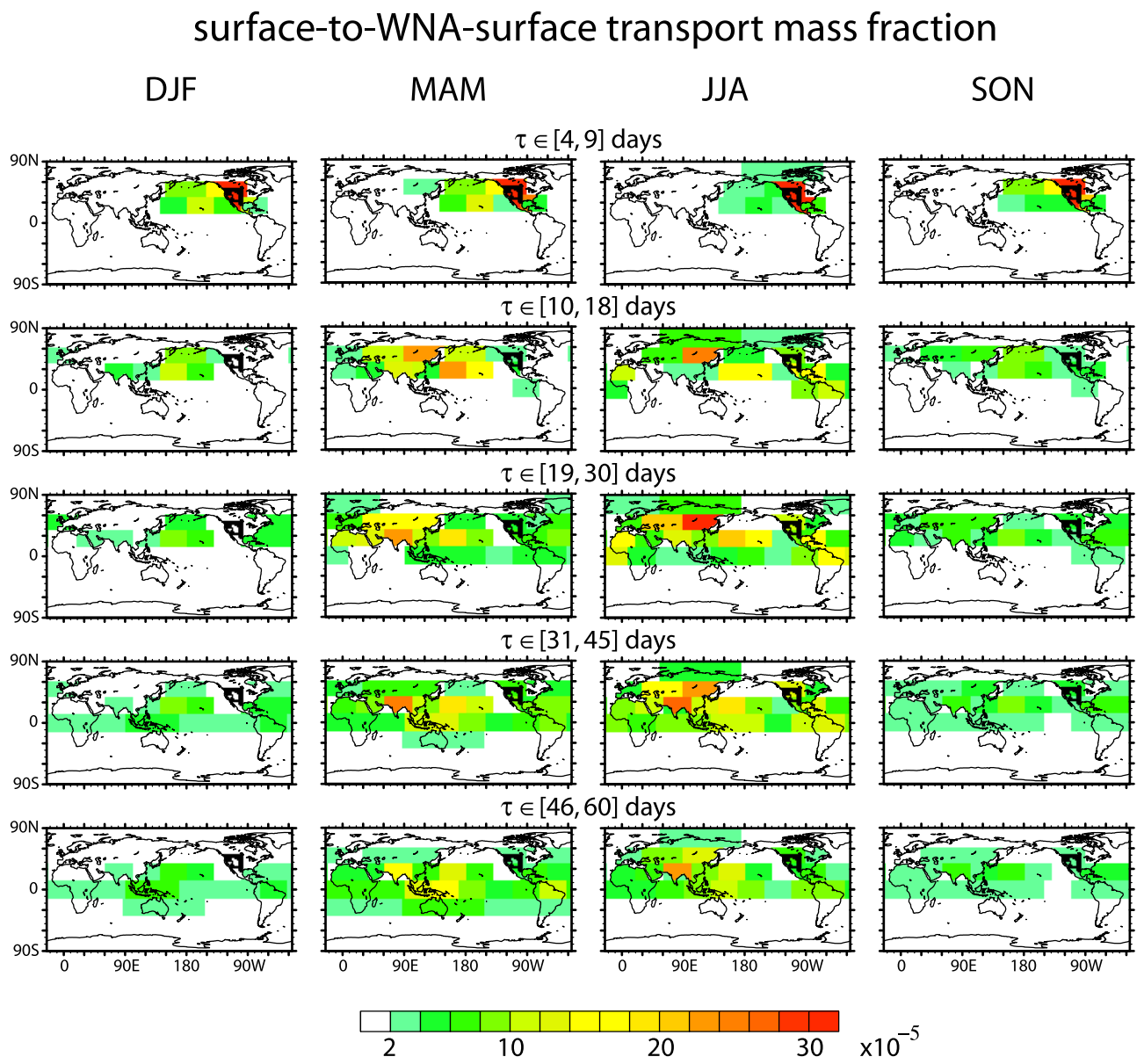

Figure 8. The Ω_i-to-Ω_{WNA} transport mass fraction associated with each Ω_i for the surface-to-surface transport time, τ (the atmospheric residence time), in the interval indicated. The WNA receptor region, excluding terrain above 1800 m elevation, is indicated in black.

receptor, as expected: One can show that the singularity of the surface flux (see section 3.2) at $\tau = 0$ implies that the distribution $\mathcal{R}$ has an integrable singularity at $\tau = 0$ due to eddy-diffusive transport if Ω_i and Ω_r overlap [*Primeau and Holzer*, 2006]. Figure 9 shows that the contributions to $\sum_i \langle \mathcal{R} \rangle \, \Delta t'$ from overlapping patches have mostly decayed after a residence time of ~6 d, with the exception of SEA in JJA. The slower decay for SEA in summer is consistent with the fact that air from SEA's overlapping patches is convectively injected in JJA into a middle and upper troposphere of exceptionally weak winds. This air can therefore linger aloft longer than usual before making surface contact with SEA. For patches that do not overlap the receptor, $\mathcal{R} \to 0$ as $\tau \to 0$, because transport between nonoverlapping patches takes finite time.

[50] The dominant seasonal mean teleconnections for nonoverlapping patches and the residence-time intervals of their dominance, as identified from $\mathcal{R}$, are summarized in Table 1. For this purpose, we define the dominant, nonoverlapping, nonabutting source patches for a given receptor as those for which the maximum of $\mathcal{R}$ as a function of τ stands out, by at least a factor of 1.35, above the maxima of the other $\mathcal{R}$ curves. The land and ocean parts of land-ocean partitioned patches are treated as separate patches. The corresponding residence-time interval of dominance is defined as the approximate range of τ for which the dominant $\mathcal{R}$ versus τ curves lie above the maximum of all other $\mathcal{R}$ curves. (Individual $\mathcal{R}$ curves were used to avoid visual difficulties that result from the vertical shearing of the stacked bands of Figure 9 at small τ.) No such dominant

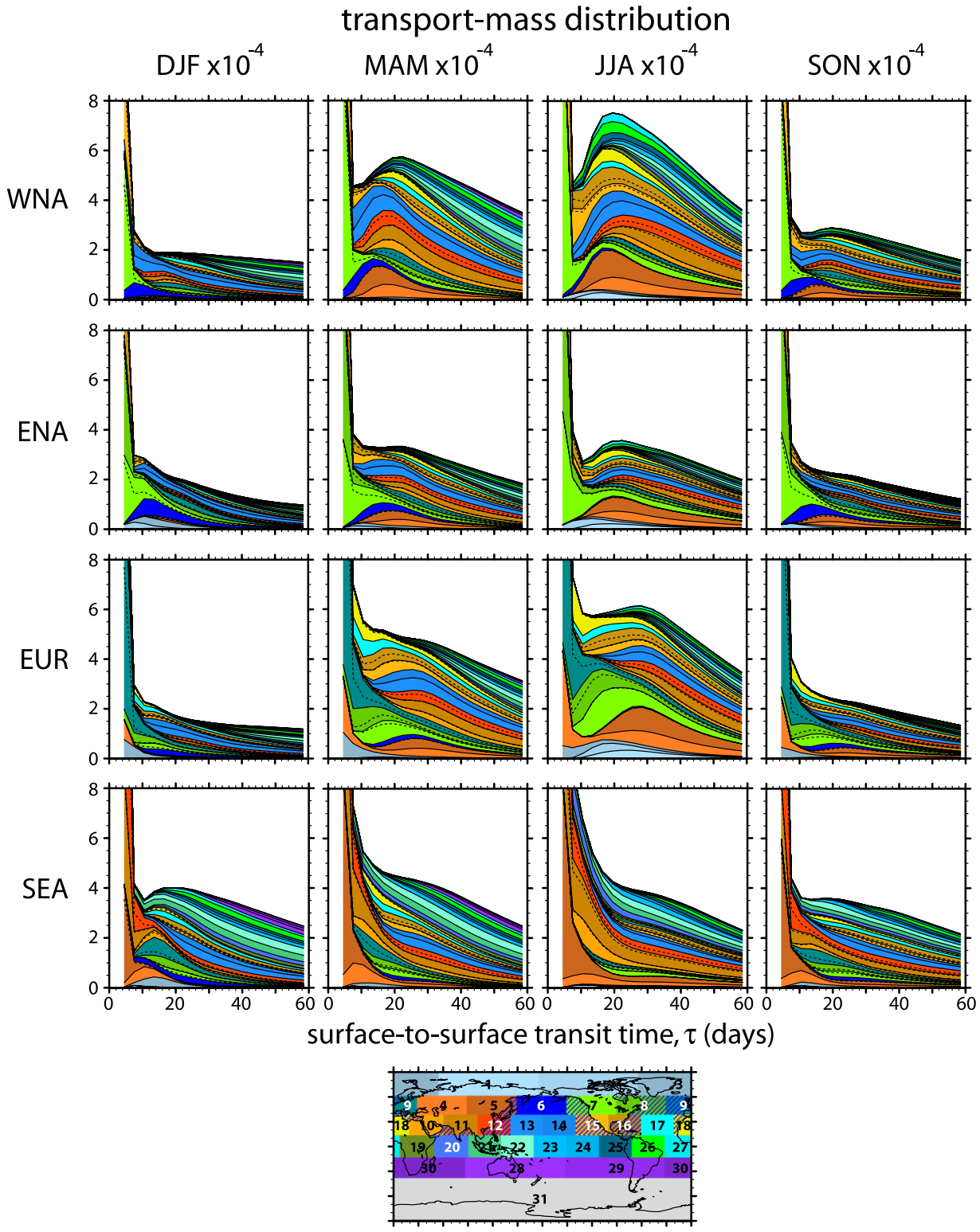

Figure 9. The seasonal mean transport mass fraction of the atmosphere in each 3-d transit-time interval that will make first surface contact with the receptor patch, Ω_r, as a function of residence time, τ, for the receptors and seasons indicated. The contributions from each source patch, Ω_i, are stacked sequentially from Ω_1 to Ω_{31}. The width of each vertical band is equal to $\langle \mathcal{R}(\tau, \Omega_i, \Omega_r; t) \rangle \Delta t'$ so that the top-most curve gives the sum over all source patches, $\sum_i \langle \mathcal{R} \rangle \Delta t'$. The dashed lines subdivide bands into contributions that had last surface contact with the land (below the dashed line) and ocean (above the dashed line) parts of the surface patch.

Table 1. Dominant $\Omega_i \rightarrow \Omega_r$ Transport Teleconnections for Nonoverlapping, Nonabutting Source and Receptor Patches, as Determined From the Transport Mass Distribution $\mathcal{R}$[a]

	DJF		MAM		JJA		SON	
Ω_r	Ω_i	Days	Ω_i	Days	Ω_i	Days	Ω_i	Days
WNA	Ω_6	5–18	Ω_5^L	12–20	Ω_5^L	13–31	Ω_6	7–14
	Ω_{13}	7–43	Ω_{13}	9–19				
	Ω_{14}	4–17	Ω_{14}	7–14				
ENA	Ω_6	9–24	–	–	Ω_5^L	16–36	Ω_6	9–19
	Ω_7^O	6–15					Ω_7^O	7–14
EUR	Ω_3	4–10	Ω_3	4–10	Ω_5^L	22–45	Ω_3	4–11
			Ω_7^L	13–22	Ω_7^L	11–31	Ω_7^L	11–22
			Ω_8^O	6–14	Ω_8^L	9–20	Ω_8^O	5–16
			Ω_{17}	6–15				
SEA	–	–	Ω_4	6–15	Ω_{10}^L	9–20	Ω_4	6–15
					Ω_{20}	4–15		

[a]The approximate residence-time interval of dominance is indicated in days.

contributions were identified for SEA in DJF and for ENA in MAM, because a number of patches make large contributions that are not well separated from the others (see Figure 9).

[51] For WNA and ENA, North Pacific air dominates in winter and fall, consistent with active wintertime Pacific storm tracks. The rapid transport by the westerly winds appears to compensate for strong isentropic mixing which is expected to bring a fraction of this air into surface contact before reaching the receptor. In spring WNA still receives large amounts of North Pacific air, but convection over Asia begins to deliver also large amounts of Siberian Ω_5^L air. In summer the WNA, ENA, and EUR surfaces receive large fractions of Siberian Ω_5^L air, and EUR also receives North American Ω_7^L and Ω_8^L air, consistent with strong summertime continental convection providing conduits both from and to the surface. During fall and spring, EUR receives dominantly NW North Atlantic Ω_8^O air and western North American Ω_7^L air, with central North Atlantic Ω_{17} air also making large contributions in spring. During all seasons except summer, Arctic Ω_3 air also makes dominant contributions to EUR at relatively short residence times, because of the fact that the Arctic Ω_3 patch nearly abuts the EUR receptor patch. The dominant remote contributions for SEA are consistent with the seasonality of the Asian monsoon circulation: In summer Middle Eastern Ω_{10}^L and Indian Ocean Ω_{20} air dominate, while in spring and fall central Asian Ω_4 air dominates.

5. Discussion and Conclusions

[52] It has been our goal to diagnose the troposphere's long-range transport in a tracer-independent way, not to simulate any particular chemical constituent, or even any idealized surrogate for chemical constituents. To that end, we have employed the boundary propagator, $\mathcal{G}$. The propagator $\mathcal{G}$ is the Green function for surface mixing ratio, as opposed to surface fluxes, and has the compelling interpretation of being the joint distribution of transit times and surface locations since an air parcel last made surface contact. We have calculated $\mathcal{G}(\mathbf{r}, t|\Omega_i, t')$ using MATCH driven by NCEP reanalysis data for field times t from September 1998 to August 2001, with a 3-d resolution in source time t', and hence transit time, and a 41-patch resolution in last-contact location, Ω_i. The resulting ensemble of boundary propagators (one realization for each 3-d field-time average) represents the partitioning of air at every location and every time into transit time since last surface contact and region of that contact.

[53] We have analyzed the climatological, seasonal mean global boundary propagator for four high-population receptor regions: western and eastern North America (WNA, ENA), Europe (EUR), and Southeast Asia (SEA). The column burden of $\mathcal{G}$ quantifies the contributions of remote surface origin to the free troposphere over the receptor, the surface flux of $\mathcal{G}$ gives the flux of newly arriving remote origin air onto the receptor surface, and the transport mass distribution $\mathcal{R}$, which is the residence-time partitioned mass fraction of the atmosphere in transit from source to receptor, provides a novel characterization of surface-to-surface transport teleconnections. Our analysis has identified a number of key features of tropospheric global-scale transport:

[54] 1. The transit-time dependence of the dominant locations of last surface contact displays pronounced seasonality. For example, for the WNA receptor in winter and spring strong mixing on sloping isentropes over the Pacific causes the dominant last-contact patch to propagate with increasing transit time eastward across the Pacific surface. In contrast, in summer the troposphere is more stable over the Pacific so that air above the boundary layer is less likely to make contact with the Pacific surface. In summer, the dominant last-contact regions therefore "hop" across the ocean to continental Asia.

[55] 2. The surface origin of air does not homogenize zonally at long transit times. The efficiency with which air escapes the source patch and is mixed again to the surface en route to the receptor depends on boundary layer mixing, frontal activity, and deep convection, all of which are distributed highly inhomogeneously.

[56] 3. A nearly universal pattern of last surface contact that is only weakly dependent on receptor emerges at the longest transit times considered ($\sim$2 months). The dominant last-contact patches of that pattern coincide with the primary regions of tropical deep convection and/or the Tibetan plateau, depending on season. This is because air attains long transit times to midlatitude receptors by being injected into the upper tropical troposphere so that it is shielded from immediate access to rapid isentropic transport to the surface.

[57] 4. The surface-origin composition of the burden over the receptors studied changes only slowly after a transit time of $\sim$ 6 weeks in DJF and SON, when the Northern Hemisphere Underworld has its greatest southward extent allowing for the most rapid mixing of remote air to the surface, and hence the most rapid equilibration of surface-origin composition.

[58] 5. Northern midlatitude patches have the expected land-ocean contrast, with air that had last contact with the ocean dominating in winter, and air that had last contact with land dominating in summer. For the more southern midlatitude patches the relative importance of the ocean component is influenced by whether the ocean region encompasses the climatological starting points of warm conveyor belts, which provide access to the free tropo-

sphere, or regions of the climatological subtropical highs, where subsidence hinders access to the free troposphere.

[59] 6. The flux of newly arriving air onto the receptor surface and the column burden above the receptor have distinct surface-origin compositions. Air from different surface patches can experience very different pathways and vertical mixing en route to the receptor resulting in different vertical profiles, and hence different efficiencies of mixing to the receptor surface. The following contrasts between receptor burdens and fluxes were identified: (1) east Asian and European air contribute comparably to the flux onto eastern North America (ENA), in spite of east Asian air dominating European air in the column burden over ENA. (2) At their respective modes, the flux of European air onto SE Asia is just as large as (JJA), or larger than (DJF, MAM, and SON), the flux of SE Air onto Europe, in spite of SE Asian air burdens over Europe being larger than European air burdens over SE Asia. (3) The percentage contribution of Arctic air to the flux of newly arriving air is much larger than its nearly negligible percentage contribution to the burden, because Arctic air generally arrives over midlatitude receptors at low levels.

[60] 7. At transit times of only several days the surface-origin partition of the flux of newly arriving air is nearly identical to that of the burden and dominated by air from patches overlapping the receptor region. At transit times of $\sim$60 d, the surface-origin composition of the flux has not equilibrated and is changing faster than that of the burden because transport to the midlatitude surface takes more time than transport to the midlatitude free troposphere. This is especially true for equatorial and Southern Hemisphere air, which has to traverse the Middleworld to the NH Underworld to have isentropic access to the receptors studied.

[61] 8. The transport mass distribution, $\mathcal{R}$, is particularly effective for identifying surface-to-surface teleconnections as a function of atmospheric residence time, τ, that is, the time between successive surface contacts. The corresponding average surface-to-surface flux per unit residence time is proportional to $\mathcal{R}/\tau$. The mass fraction making first contact with a given receptor regardless of surface origin is strongly correlated with the model's planetary boundary layer height, consistent with deep boundary layers providing conduits of efficient mixing to the surface. Correspondingly, the mass fraction of the atmosphere making first contact with the continental receptors studied is largest in summer and spring.

[62] **Acknowledgment.** This work was supported by NSF grant ATM-04-32514.

References

Berntsen, T. K., S. Karlsdottir, and D. A. Jaffe (1999), Influence of Asian emissions on the composition of air reaching the northwestern United States, *Geophys. Res. Lett.*, *26*, 2171–2174.

Bey, I., D. J. Jacob, R. M. Yantosca, J. A. Logan, B. D. Field, A. M. Fiore, Q. Li, H. Y. Liu, L. J. Mickley, and M. G. Schultz (2001), Global modeling of tropospheric chemistry with assimilated meteorology: Model description and evaluation, *J. Geophys. Res.*, *106*, 23,073–23,095.

Cooper, O. R., et al. (2004), A case study of transpacific warm conveyor belt transport: Influence of merging airstreams on trace gas import to North America, *J. Geophys. Res.*, *109*, D23S08, doi:10.1029/2003JD003624.

Hack, J. J. (1994), Parameterization of moist convection in the NCAR Community Climate Model, CCM2, *J. Geophys. Res.*, *99*, 5551–5568.

Hall, T. M., and M. Holzer (2003), Advective-diffusive mass flux and implications for stratosphere-troposphere exchange, *Geophys. Res. Lett.*, *30*(5), 1222, doi:10.1029/2002GL016419.

Haine, T. W. N., and T. M. Hall (2002), A generalized transport theory: Water-mass composition and age, *J. Phys. Oceanogr.*, *32*, 1932–1946.

Heald, C. L., et al. (2003), Asian outflow and trans-Pacific transport of carbon monoxide and ozone pollution: An integrated satellite, aircraft, and model perspective, *J. Geophys. Res.*, *108*(D24), 4804, doi:10.1029/2003JD003507.

Heald, C. L., D. J. Jacob, R. J. Park, B. Alexander, T. D. Fairlie, R. M. Yantosca, and D. A. Chu (2006), Transpacific transport of Asian anthropogenic aerosols and its impact on surface air quality in the United States, *J. Geophys. Res.*, *111*, D14310, doi:10.1029/2005JD006847.

Holzer, M. (1999), Analysis of passive tracer transport as modeled by an atmospheric general circulation model, *J. Clim.*, *12*, 1659–1684.

Holzer, M., and T. M. Hall (2000), Transit-time and tracer-age distributions in geophysical flows, *J. Atmos. Sci.*, *57*, 3539–3558.

Holzer, M., and T. M. Hall (2007), Low-level transpacific transport, *J. Geophys. Res.*, *112*, D09103, doi:10.1029/2006JD007828.

Holzer, M., and F. W. Primeau (2006), The diffusive ocean conveyor, *Geophys. Res. Lett.*, *33*, L14618, doi:10.1029/2006GL026232.

Holzer, M., I. G. McKendry, and D. A. Jaffe (2003), Springtime trans-Pacific atmospheric transport from east Asia: A transit-time-pdf approach, *J. Geophys. Res.*, *108*(D22), 4708, doi:10.1029/2003JD003558.

Holzer, M., T. M. Hall, and R. B. Stull (2005), Seasonality and weather-driven variability of transpacific transport, *J. Geophys. Res.*, *110*, D23103, doi:10.1029/2005JD006261.

Hoskins, B. J. (1991), Towards a PV-θ view of the general circulation, *Tellus, Ser. AB*, *43*, 27–35.

Huntrieser, H., et al. (2005), Intercontinental air pollution transport from North America to Europe: Experimental evidence from airborne measurements and surface observations, *J. Geophys. Res.*, *110*, D01305, doi:10.1029/2004JD005045.

Husar, R. B., et al. (2001), Asian dust events of April 1998, *J. Geophys. Res.*, *106*, 18,317–18,330.

Jacob, D. J., J. A. Logan, and P. P. Murti (1999), Effect of rising Asian emissions on surface ozone in the United States, *Geophys. Res. Lett.*, *26*, 2175–2178.

Jacob, D. J., J. H. Crawford, M. M. Kleb, V. S. Connors, R. J. Bendura, J. L. Raper, G. W. Sachse, J. C. Gille, L. Emmons, and C. L. Heald (2003), Transport and Chemical Evolution over the Pacific (TRACE-P) aircraft mission: Design, execution, and first results, *J. Geophys. Res.*, *108*(D20), 9000, doi:10.1029/2002JD003276.

Jaeglé, L., D. A. Jaffe, H. U. Price, P. Weiss-Penzias, P. I. Palmer, M. J. Evans, D. J. Jacob, and I. Bey (2003), Sources and budgets for CO and O_3 in the northeastern Pacific during the spring of 2001: Results from the PHOBEA-II Experiment, *J. Geophys. Res.*, *108*(D20), 8802, doi:10.1029/2002JD003121.

Jaffe, D., et al. (1999), Transport of Asian air pollution to North America, *Geophys. Res. Lett.*, *26*, 711–714.

Jaffe, D., I. G. McKendry, T. Anderson, and H. Price (2003), Six 'new' episodes of trans-Pacific transport of air pollutants, *Atmos. Environ.*, *37*, 391–404.

Kalnay, E., et al. (1996), The NMC/NCAR 40-year reanalysis project, *Bull. Am. Meteorol. Soc.*, *77*, 437–471.

Kistler, R., et al. (2001), The NCEP/NCAR 50-year reanalysis, *Bull. Am. Meteorol. Soc.*, *82*, 247–267.

Liang, Q., L. Jaeglé, D. A. Jaffe, P. Weiss-Penzias, A. Heckman, and J. A. Snow (2004), Long-range transport of Asian pollution to the northwest Pacific: Seasonal variations and transport pathways of carbon monoxide, *J. Geophys. Res.*, *109*, D23S07, doi:10.1029/2003JD004402.

Liang, Q., L. Jaeglé, and J. M. Wallace (2005), Meteorological indices for Asian outflow and transpacific transport on daily to interannual timescales, *J. Geophys. Res.*, *110*, D18308, doi:10.1029/2005JD005788.

Liu, J., D. L. Mauzerall, and L. W. Horowitz (2005), Analysis of seasonal and interannual variability in transpacific transport, *J. Geophys. Res.*, *110*, D04302, doi:10.1029/2004JD005207.

Luo, C., N. M. Mahowald, N. Meskhidze, Y. Chen, R. L. Siefert, A. R. Baker, and A. M. Johansen (2005), Estimation of iron solubility from observations and a global aerosol model, *J. Geophys. Res.*, *110*, D23307, doi:10.1029/2005JD006059.

Newell, R. E., and M. J. Evans (2000), Seasonal changes in pollutant transport to the North Pacific: The relative importance of Asian and European sources, *Geophys. Res. Lett.*, *27*, 2509–2512.

Parrish, D. D., Y. Kondo, O. R. Cooper, C. A. Brock, D. A. Jaffe, M. Trainer, T. Ogawa, G. Hübler, and F. C. Fehsenfeld (2004), Intercontinental Transport and Chemical Transformation 2002 (ITCT 2K2) and Pacific Exploration of Asian Continental Emission (PEACE) experiments: An overview of the 2002 winter and spring intensives, *J. Geophys. Res.*, *109*, D23S01, doi:10.1029/2004JD004980.

Peacock, S., and M. Maltrud (2006), Transit-time distributions in a global ocean model, *J. Phys. Oceanogr.*, *36*, 474–495.

Plumb, R. A., and J. D. Mahlman (1987), The zonally averaged transport characteristics of the GFDL general circulation model, *J. Atmos. Sci.*, *44*, 298–327.

Primeau, F. (2005), Characterizing transport between the surface mixed layer and the ocean interior with a forward and adjoint global ocean transport model, *J. Phys. Oceanogr.*, *35*, 545–564.

Primeau, F. W., and M. Holzer (2006), The ocean's memory of the atmosphere: Residence-time and ventilation-rate distributions of water masses, *J. Phys. Oceanogr.*, *36*, 1439–1456, doi:10.1175/JPO2919.1.

Prospero, J. M. (1999), Long-term measurements of the transport of African mineral dust to the southeastern United States: Implications for regional air quality, *J. Geophys. Res.*, *104*, 15,917–15,927.

Prospero, J. M., R. A. Glaccum, and R. T. Nees (1981), Atmospheric transport of soil dust from Africa to South America, *Nature*, *289*, 570–572.

Rasch, P. J. and M. Lawrence (1998), Recent developments in transport methods at NCAR, in *MPI Workshop on Conservative Transport Schemes*, vol. 265, pp. 65–75, Max-Planck-Inst. for Meteorol., Hamburg, Germany.

Rasch, P. J., N. M. Mahowald, and B. E. Eaton (1997), Representations of transport, convection and the hydrologic cycle in chemical transport models: Implications for the modeling of short lived and soluble species, *J. Geophys. Res.*, *102*, 28,127–28,138.

Stohl, A. (2001), A one-year Lagrangian "climatology" of airstreams in the Northern Hemisphere troposphere and lowermost stratosphere, *J. Geophys. Res.*, *106*, 7263–7279.

Stohl, A., and T. Trickl (1999), A textbook example of long-range transport: Simultaneous observations of ozone maxima of stratospheric and North American origin in the free troposphere over Europe, *J. Geophys. Res.*, *104*, 30,445–30,462.

Stohl, A., S. Eckhardt, C. Forster, P. James, and N. Spichtinger (2002), On the pathways and timescales of intercontinental air pollution transport, *J. Geophys. Res.*, *107*(D23), 4684, doi:10.1029/2001JD001396.

Wenig, M., N. Spichtinger, A. Stohl, G. Held, S. Beirle, T. Wagner, B. Jähne, and U. Platt (2002), Intercontinental transport of nitrogen oxide pollution plumes, *Atmos. Chem. Phys.*, *3*, 387–393.

Yienger, J. J., M. Galanter, T. A. Holloway, M. J. Phadnis, S. K. Guttikunda, G. R. Carmichael, W. J. Moxim, and H. Levy II (2000), Episodic nature of air pollution transport from Asia to North America, *J. Geophys. Res.*, *105*, 26,931–26,945.

Zhang, G. J., and N. A. McFarlane (1995), Sensitivity of climate simulations to the parameterization of cumulus convection in the Canadian Climate Centre general circulation model, *Atmos. Ocean*, *33*, 407–446.

T. M. Hall and M. Holzer, NASA Goddard Institute for Space Studies, 2880 Broadway, New York, NY 10025, USA. (thall@giss.nasa.gov; hm2220@columbia.edu)